

Dear Raphael,

Thank you for reviewing our manuscript a second time. Our paper has improved from these two rounds of constructive comments.

Please see our replies below (reviewer comments italicized):

*1. The signal remains quite weak in the observational period, due to the influence of internal variability and the relatively weak eruptions with still uncertain forcing. The authors have pointed out this in the text, with some additional paragraphs in the revised version. I think it is worth mentioning this caveat in the abstract (potentially accompanied by the argument that the LM model analysis is helpful in this regard thanks to the larger number of eruptions available and possibility to quantify the (internal-)noise component).*

Agreed. We have modified our abstract to discuss the caveat of the L20 (historic) eruptions yielding inconclusive results.

*2. Are the correlation values in Figure 9 correct? From the Figure, I would rather expect significant values in both seasons for temperature and non-significant correlation for DJF-precip. Is it possible that the numbers got mixed up here or did I get something wrong?*

The correlation values previously reported were correct, and are slightly altered in the new text due to a more consistent spatial domain averaging (see comment #3 below).

The temperature response is indeed significant in JJA (in the northern South American domain) in response to volcanic forcing, but when this spatially averaged temperature is plotted against the spatially averaged isotopic signal (using 45 volcanic events in the regression), there is a weak and non-significant relation. We argued in the text that precipitation reduction in northern South America is instead the dominant contributor to the isotopic enrichment that we see during this season/location. During DJF, we believe both temperature and precipitation are important in driving the isotopic signal, although the two factors seem to be driving it in opposite directions. In the spatial composite or in a multiple linear regression, the temperature effect “wins” (unlike JJA) if only those two predictors are used. We have added a supplementary Figure S7, reproduced below, to our manuscript and added text in section 3.2.3 to further support this interpretation.

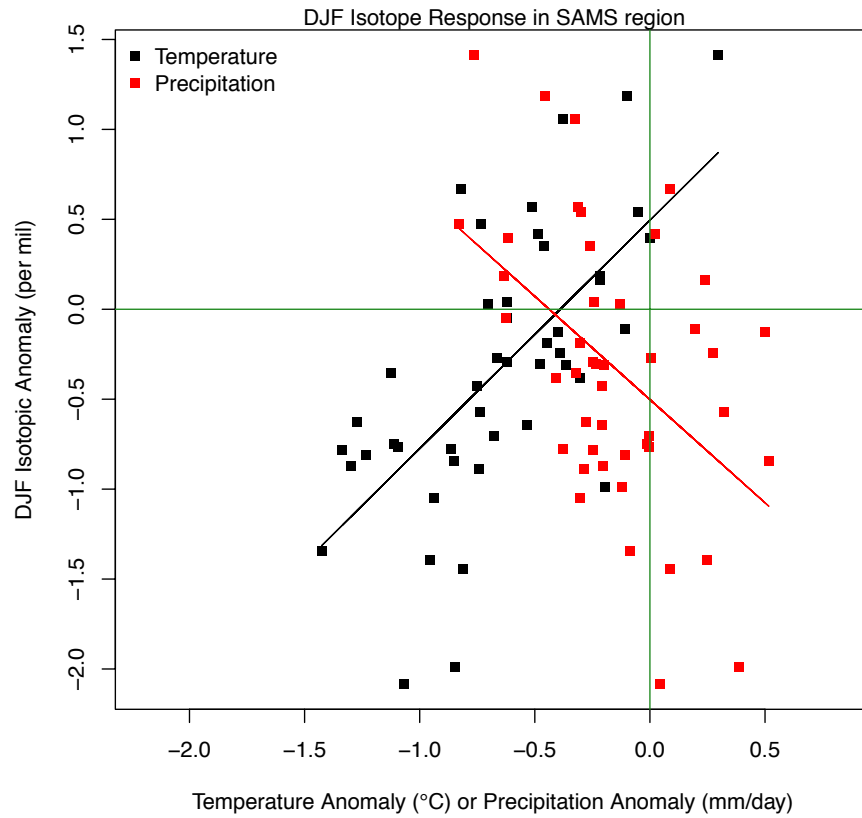


**Fig. S7.** Regression of spatially-averaged DJF  $\delta^{18}\text{O}_p$  anomaly vs. temperature (black squares) or precipitation (red squares). The regression uses all 45 LM volcanic events and averaging is done over the SAMS domain defined in the text. Black and red lines are the corresponding (least-squares) regression lines.

3. I am a bit surprised by the weak signal in Fig. 12 bottom-right panel (isotopic response in JJA). This was not well visible in the figure in the first submission, so it did not call my attention. The purple square is hardly outside the range of values from the control simulation. In Fig. 10 the values seem to be quite large (mostly above 0.3 over the domain considered), so the value of ca. 0.15 in Fig. 12 appears to be too low. Is this because the northern part of the selected domain is affected by the negative values seen over the Atlantic? Would this make it worth moving the northern limit 1-2 degrees south to have a more consistent domain?

56 *If not, I think it's worth noting in the text that the signal is only marginally larger than*  
57 *internal variability for this specific season and variable.*  
58  
59 Thank you for pointing this out. We agree that our choice of domain was not optimal.  
60 We have changed the averaging domain, which now yields a larger JJA isotopic  
61 signal (Figure 12, bottom right) that is easier to reconcile with the large signal in the  
62 spatial composite (Figure 10). Figures 2 and 9 have been re-plotted and domains  
63 redefined throughout the text for consistency.  
64

65 The influence of volcanic eruptions on the climate of tropical South America during the  
66 last millennium in an isotope-enabled GCM

67 **Christopher M. Colose<sup>1</sup>, Allegra N. LeGrande<sup>2</sup>, Mathias Vuille<sup>1</sup>**

68

69 [1] Dept. of Atmospheric & Environmental Sciences, University at Albany, SUNY,  
70 Albany, NY 12222

71 [2] NASA Goddard Institute for Space Studies, New York, NY, 10025

72 Correspondence to: Christopher Colose (ccolose@albany.edu)

73

74

75

76

77

78

79

80

81

82

83

84

85

86

87

## Abstract

Currently, little is known on how volcanic eruptions impact large-scale climate phenomena such as [South American](#) paleo-ITCZ position [and](#), summer monsoon behavior. In this paper, an analysis of observations and model simulations is employed to assess the influence of large volcanic eruptions on the climate of tropical South America. This problem is [first](#) considered [for](#) historically recent volcanic episodes [for](#) which more comprehensive global observations exist, [but also where fewer events and the confounding effects of ENSO lead to inconclusive interpretation of the impact of volcanic eruptions at the continental scale.](#) Therefore, we also examine a greater number [of](#) reconstructed volcanic events for the period 850 C.E. to present that are incorporated into the NASA GISS ModelE2-R simulation of the Last Millennium.

An advantage of this model is its ability to explicitly track water isotopologues throughout the hydrologic cycle and simulating the isotopic imprint following a large eruption. This effectively removes a degree of uncertainty associated with error-prone conversion of isotopic signals into climate variables, and allows for a direct comparison between GISS simulations and paleoclimate proxy records.

Our analysis reveals that both precipitation and oxygen isotope variability respond with a distinct seasonal and spatial structure across tropical South America following an eruption. During austral winter, the heavy oxygen isotope in precipitation is enriched, likely due to reduced moisture convergence in the ITCZ domain and reduced rainfall over northern South America. During austral summer, however, precipitation is depleted in heavy isotopes over Amazonia, despite reductions in rainfall, suggesting that the isotopic

Allegra N LeGrande 2/19/2016 8:37 AM

**Deleted:** or

Allegra N LeGrande 2/19/2016 8:37 AM

**Deleted:** South American

Chris Colose 2/17/2016 9:51 PM

**Deleted:** both

Chris Colose 2/17/2016 9:54 PM

**Deleted:** ,

Chris Colose 2/19/2016 5:53 PM

**Deleted:** yield more and

Allegra N LeGrande 2/19/2016 8:41 AM

**Deleted:** s

Chris Colose 2/19/2016 5:54 PM

**Deleted:** the

Allegra N LeGrande 2/19/2016 8:41 AM

**Deleted:** s

Chris Colose 2/17/2016 9:52 PM

**Deleted:** as well as

response is not a simple function of the ‘amount effect.’ During the South American monsoon season, the amplitude of the temperature response to volcanic forcing is larger than the rather weak and spatially less coherent precipitation signal, complicating the isotopic response to changes in the hydrologic cycle.

## 1. Introduction

## 1.1. Volcanic Forcing on Climate

Plinian (large, explosive) volcanic eruptions are a dominant driver of naturally forced climate variability during the Last Millennium (LM, taken here to be 850 C.E. to present; e.g., Stothers and Rampino, 1983; Hansen et al., 1992; Crowley et al., 2000; Robock et al., 2000; Robock, 2003; Goosse et al., 2005; Yoshimori et al., 2005; Emile-Geay et al., 2008; Cole-Dai, 2010; Timmreck, 2012; Iles et al., 2013; Schurer et al., 2014). In addition to their importance for 20<sup>th</sup> century climate, they are the largest magnitude external forcing during last 1000 years of the pre-industrial period, the most recent key interval identified by the Paleoclimate Modelling Intercomparison Project Phase III (PMIP3). As such, these eruptions serve as a natural testbed to assess the skill of climate models in simulating how climate responds to external perturbations.

Although the most significant climate impacts of eruptions are realized over just a few years following the eruption, they provide the source of the largest amplitude perturbations to Earth's energy budget during the LM. For example, the eruption of Mt. Pinatubo in June 1991, although transitory, exerted a radiative forcing comparable to an instantaneous halving of atmospheric CO<sub>2</sub> [Hansen et al., 1992; Minnis et al., 1993; see also Driscoll et al. (2012) for models in the Coupled Model Intercomparison Project Phase 5 (CMIP5)]; several paleo-eruptions during the LM likely had an even larger global impact (Figure 1).

The principle climate impact from volcanic eruptions results from the liberation of sub-surface sulfur-containing gases such as sulfur dioxide, which are injected into the

Allegra N LeGrande 2/19/2016 8:51 AM  
**Deleted:** and hydrogen sulfide

stratosphere and react with water to form sulfate aerosols (e.g., Harshvardhan and Cess, 1976; Coakley and Grams, 1976; Pollack et al., 1976, 1981; Lacis et al., 1992). The most pronounced impact of large tropical eruptions includes a radiatively cooled troposphere and heated stratosphere (e.g., Lacis et al., 1992; Robock and Mao, 1995; Stenchikov et al., 1998). Sulfate aerosols from the Mt. Pinatubo eruption grew from a background effective radius of  $\sim 0.2 \mu\text{m}$  up to  $\sim 0.8 \mu\text{m}$ , strongly scattering incoming solar radiation. For sulfate aerosols in this size range, this shortwave scattering is 5-10x larger than the increase in infrared opacity from the aerosols, and results in a warming stratosphere and cooling of Earth's surface (Turco et al., 1982; Lacis et al., 1992).

Studies on the impacts of volcanic eruptions have generally focused on global or Northern Hemisphere metrics (e.g., Lucht et al., 2002; Gillett et al., 2004; Shindell et al., 2004; Oman et al., 2005; Oman et al., 2006; Anchukaitis et al., 2010; Peng et al., 2010; Evan et al., 2012; Zhang et al., 2013; Man et al., 2014), for instance in examining responses to the East Asian monsoon system (EAMS) or the Arctic Oscillation. Comparatively little attention has been given to the Southern Hemisphere, or to South America specifically (although see Joseph and Zeng, 2011, and Wilmes et al., 2012). Some previous work has focused on the Southern Annular Mode in the ERA-40 and NCEP/NCAR reanalysis, in addition to a previous version of NASA Goddard Institute for Space Studies (GISS) Model-E (Robock et al., 2007) and in a subset of CMIP3 models (Karpechko et al., 2010) or in CMIP5 (Gillett and Fyfe, 2013).

How volcanic forcing is expressed over South America remains an important target question for several reasons. First, recognition of the South American monsoon system (SAMS) as an actual monsoon system is less than two decades old (Zhou and Lau,

1998), and thus study of SAMS dynamics is still relatively young (section 1.3) and very little work has been done specifically focused on volcanic eruptions. For instance, should we expect to see a reduction in austral summer rainfall (during the monsoon season) as has been reported for the EAMS (Man et al., 2014)? Secondly, the largest volcanic eruptions during the late 20<sup>th</sup> century (e.g., Mt. Agung, 1963, Indonesia; El Chichón, 1982, Mexico; Mt. Pinatubo, 1991, Island of Luzon in the Philippines- hereafter, these three events are referred to as L20 eruptions) occur quasi-simultaneously with an anomalous El Niño-Southern Oscillation (ENSO) state, and in general represent a small sample size in a noisy system. This limits the prospect of robust hypothesis testing and guidance for what impacts ought to be expected following large eruptions at the continental scale. Finally, South America offers promise for a comparatively dense network of high-resolution proxy locations relative to other tropical regions (see below), offering the potential to detect whether South American hydroclimate signals to large eruptions are borne out paleoclimatically.

In this study, we explore the post-volcanic response of South American climate operating through the vehicle of unique model simulations (spanning the LM) using the recently developed GISS ModelE2-R (LeGrande et al., 2015, in prep; Schmidt et al., 2014a), which allows for the sampling of a greater number of events than is possible over the instrumental period. Emphasis is placed on temperature and precipitation, but a novel part of this study extends to the response of water isotopologues (e.g., H<sub>2</sub><sup>18</sup>O) [colloquially referred to hereafter as ‘isotopes’ and expressed as  $\delta^{18}\text{O}$  in units per mil (‰) vs. Vienna Standard Mean Ocean Water]. The isotopic composition of precipitation

( $\delta^{18}\text{O}_p$ ) is a key variable that is directly derived from proxy data used in tropical paleoclimate reconstructions.

The aim of this paper is to create a potentially falsifiable prediction for the isotopic imprint that a volcanic eruption should tend to produce across the South American continent. The ability to explicitly model the isotopic response allows for a less ambiguous comparison of simulations and paleoclimate records and for hypothesis testing. It is unclear whether or not the current proxy archives are suitable to test such a prediction with high confidence, given dating uncertainties (in both proxies and in the actual timing of eruptions), or the level of noise in proxy data and the real world. Additionally, the prevailing high-resolution archives in South America only feature a few tropical records (Vimeux et al., 2009; Neukom and Gergis, 2012; Vuille et al., 2012). Nonetheless, the growing number of high-resolution records offers hope that testing the modeled response to high-frequency volcanic signals will be an avenue for future research. This can also better inform debate centered on the inverse problem in interpreting isotopic signals (i.e., what do observed changes in proxy data imply about past climate changes?), which remains contentious (section 1.4).

The structure of this article is as follows: in the remaining part of section 1, we summarize previous literature on the impact of large volcanic eruptions on paleoclimate, in addition to a discussion of South American climate. Section 2 presents data and methodology, including how volcanic forcing is implemented in ModelE2-R. Section 3 discusses our results and we end with conclusions in section 4.

## 1.2. Volcanic forcing during the Last Millennium

235

236 Volcanic forcing has had a very large influence on the climate of the LM  
237 (Crowley, 2000; Hegerl et al., 2003; Shindell et al., 2004; Mann et al., 2005; Hegerl et al.,  
238 2006; Fischer et al., 2007; D'Arrigo et al., 2009; Timmreck, 2012; Esper et al., 2013;  
239 Ludlow et al., 2013; Schurer et al., 2014). Several studies (Miller et al., 2012; Schurer et  
240 al., 2014; Atwood et al., [2016](#); McGregor et al., 2015) collectively provide a compelling  
241 case that volcanic forcing may be substantially more important than solar forcing on a  
242 hemispheric-to-global scale during the LM, in addition to driving a large portion of the  
243 inter-annual to multi-decadal variability in LM simulations (Schmidt et al., 2014b).

244 Two volcanic forcing datasets (Gao et al., 2008; Crowley and Unterman, 2013)  
245 relying on ice core reconstructions of volcanism are used as input in the LM ModelE2-R  
246 simulations (and are the CMIP5/PMIP3 LM standard), as discussed in Section 2.

247

### 248 1.3. Tropical South American Climate

249

250 South America is home to nearly 390 million people. The continent spans a vast  
251 meridional extent (from ~10 °N to 55 °S), contains the world's largest rainforest (the  
252 Amazon), in addition to one of the driest locations on Earth (the Atacama desert). The  
253 continent has diverse orography, spanning the high Andes along the Pacific to Laguna del  
254 Carbón in Argentina, the lowest point in the Southern Hemisphere. Because of this, South  
255 America hosts a rich diversity of climate zones and biodiversity, all of which may  
256 respond in unique ways to external forcing.

257 The most prominent climatic feature of tropical and subtropical South America is

Chris Colose 2/19/2016 5:56 PM

Deleted: 2015, in press

259 the South American monsoon system (Zhou and Lau, 1998; Marengo et al., 2001; Vera et  
260 al., 2006; Garreaud et al., 2009; Marengo et al., 2012). Much of South America is in a  
261 monsoon regime, with tropical/subtropical rainfall over the continent exhibiting a  
262 pronounced seasonal cycle. Unlike other monsoon systems such as that in Asia, low-level  
263 easterly winds prevail during the entire year in tropical South America, although the wind  
264 anomalies do change direction when the annual mean wind field is removed from winter  
265 and summer composites (Zhou and Lau, 1998).

266       During austral winter, the maximum in continental precipitation is largely  
267 restricted to north of the equator, in a band-like pattern associated with the oceanic Inter-  
268 Tropical Convergence Zone (ITCZ). During austral summer, convection is displaced  
269 from northwestern South America, and a band of heavy precipitation covers much of the  
270 continent, from the southern Amazon Basin to central Brazil and northern Argentina. A  
271 distinctive feature of the SAMS is the South Atlantic Convergence Zone (SACZ), a band  
272 of cloudiness and precipitation sourced primarily from the tropical Atlantic that extends  
273 diagonally (southeastward) from the Amazon towards southeastern Brazil (Figure 2).

274       The SAMS onset occurs around the end of October and the demise between the  
275 end of March and April (e.g., Nogués-Paegle et al., 2002; Vera et al., 2006; Silva and  
276 Carvalho, 2007). The dominant mode of intraseasonal precipitation variability over South  
277 America during summer exhibits a dipole pattern (Nogués-Paegle and Mo, 1997),  
278 seesawing between the SACZ region and Southeastern South America, the latter  
279 including the densely populated La Plata basin with local economies strongly dependent  
280 on agricultural activities.

The SAMS is strongly modulated by ENSO behavior on inter-annual timescales (Vuille and Werner, 2005; Garreaud et al., 2009). In general, SAMS-affected regions of tropical South America tend to experience drier than normal conditions during El Niño, while conditions in subtropical latitudes are anomalously humid, including the southeastern part of the continent. Surface air temperatures tend to be anomalously warm in tropical and subtropical South America during El Niño events. These relationships depend somewhat on the time of year, and during La Niña events, the pattern is essentially reversed.

#### 1.4. Recent South American Monsoon reconstructions from isotopic proxies

SAMS variability spanning most of the Holocene has been diagnosed from speleothem records in the Peruvian Andes (Kanner et al., 2013) and a review focused on the last 1,000-2,000 years was given in Bird et al. (2011) and Vuille et al. (2012). In all cases, a critical piece of information that is required to properly diagnose paleo-SAMS variability is the ability to translate oxygen isotope variability from natural recorders into a physical climate signal of interest.

Early work on isotopes in ice core records from the tropical Andes detected a Little Ice Age (LIA) signal in the oxygen isotope composition of the ice, with results initially interpreted to reflect variations in local temperature due to their resemblance to ice core records from Greenland (e.g., Thompson et al., 1995, 1998) and due to their isotopic enrichment over the past 150 years, in parallel with rising global mean temperatures (Thompson et al., 2006). A temperature-dependence to oxygen isotope

variability has been long known and is particularly important in mid-to-high latitudes (Dansgaard, 1964) and is most directly related to the ratio of initial and final water vapor content of a parcel that is transported horizontally, rather than the temperature-dependence of fractionation itself (Hoffman and Heimann, 1997).

This interpretation in the tropics has been challenged through a number of observational and modeling efforts (Hardy et al., 2003; Vuille and Werner 2005; Vimeux et al., 2005, 2009; Kanner et al., 2012) which suggest that the isotopic signal is more closely related to the degree of rainout upstream in regions of intense convection (in the case of South America, over the Amazon basin). Additionally, since sea surface temperatures (SST) in the Pacific have a large influence on SAMS intensity on inter-annual timescales in the present, oxygen isotope variability over much of tropical South America is linked to the state of the equatorial Pacific (Bradley et al., 2003; Vuille et al., 2003a,b).

In regimes that are highly convective in nature as in tropical South America, empirical evidence shows that the amount of precipitation (the so-called “amount effect”, Dansgaard, 1964) rather than the condensation temperature correlates most strongly with  $\delta^{18}\text{O}_p$  variability, at least on seasonal to inter-annual time scales. In reality, however, the rainout most relevant for the oxygen isotope signal may be at a significant distance from the site where the proxy is derived, potentially complicating the use of local calibrations to climatology as a guide for  $\delta^{18}\text{O}_p$  interpretations (Schmidt et al., 2007). Isotopic concentrations are explainable as being a function of original concentration, rainout along the moisture transport path, and mixing.

The influence of precipitation amount on  $\delta^{18}\text{O}_p$ , in addition to changes in the

partitioning of precipitation sources, has also been identified on decadal to orbital timescales through speleothem records and lake sediments (Cruz et al., 2005; Van Breukelen et al., 2008; Bird et al., 2011; Kanner et al., 2012). These studies have also highlighted the role of latitudinal displacements of the ITCZ, which is ultimately the main moisture conduit for precipitation over the South American continent. Furthermore, many records collected throughout South America now provide evidence for enriched  $\delta^{18}\text{O}_p$  values during the Medieval Climate Anomaly, which is indicative of weakened SAMS convection and rainout, followed by depleted  $\delta^{18}\text{O}_p$  values, suggesting heavier rainfall during the LIA in tropical South America (Bird et al., 2011; Apaestegui et al., 2014) with an opposite response in Northeast Brazil (Novello et al., 2012). This, in turn, has been interpreted in terms of North Atlantic SST anomalies (Vuille et al., 2012; Ledru et al., 2013) and the position of the Atlantic ITCZ.

Nonetheless, oxygen isotopes respond in unique ways depending on the climate forcing of interest. Indeed, a unique, quantitative local relationship between an isotope record and any particular climate variable of interest is unlikely to hold for all timescales and prospective forcing agents (Schmidt et al., 2007) thus motivating the use of forward modeling to work in conjunction with proxy-based field data. For the remainder of this paper, we focus specifically on the volcanic forcing response.

## **2. Methodology**

### **2.1. Data**

The primary tool used in this study is the water isotope-enabled GISS ModelE2-R. ModelE2-R is a fully coupled atmosphere-ocean GCM (LeGrande et al., 2015, in prep; Schmidt et al., 2014a) that explicitly tracks stable water isotopes. The version used here is the same as the non-interactive atmospheric composition (NINT) physics version used in the CMIP5 experiments (Miller et al., 2014). The current model features 2° latitude x 2.5° longitude horizontal resolution and 40 vertical levels in the atmosphere up to 0.1 hPa, and is coupled to the Russell Ocean that conserves heat, water mass, and salt (Russell et al., 1995) at 1° x 1.25° resolution with 32 vertical levels. ModelE2-R includes stratospheric dynamics and prescribed ozone and aerosol species.

Due to uncertainties in past radiative forcing, a suite of LM simulations using ModelE2-R have been run with different combinations of plausible solar, volcanic, and anthropogenic land use histories (Schmidt et al., 2011, 2012) but with identical greenhouse gas and orbital evolution. These simulations span the period 850-2005 C.E. There are two reconstructions of past volcanic activity (Gao et al., 2008; Crowley and Unterman, 2013) that are used in six combinations of the ModelE2-R LM simulations (see the ‘past1000’ experimental design at <http://data.giss.nasa.gov/modelE/ar5/>, and below).

For the LM, three forcing combinations are available in the GISS ModelE2-R simulations that use the Crowley reconstruction for volcanic perturbations. These include Pongratz et al. (2008) [land]/ Krivova et al. (2007) [solar], Kaplan et al (2010) [land]/Krivova et al. (2007) [solar], and Pongratz et al. (2008) [land]/Steinhilber et al. (2009) [solar] (see Schmidt et al., 2011, 2012). We focus only on results from the Crowley reconstruction prior to 1850 CE due to a mis-scaling of the Gao forcing in the

model that roughly doubled the appropriate radiative forcing. For the historical period (1850-present), the volcanic forcing history is based on Sato et al. (1993) and is equivalent among the different (six) simulation members.

Water isotope tracers are incorporated into the model's atmosphere, land surface, sea ice, and ocean. These isotopes are advected and tracked through every stage of the hydrologic cycle. At each phase change (including precipitation, evaporation, ice formation or melting) an appropriate fractionation factor is applied (Schmidt et al., 2005) and all freshwater fluxes are tagged isotopically. Stable isotope results from the lineage of GISS models have a long history of being tested against observations and proxy records (e.g., Schmidt et al., 2007; LeGrande and Schmidt, 2008, 2009; Lewis et al., 2010, 2013, 2014; Field et al., 2014).

Crowley and Unterman (2013) discuss the details behind the LM Aerosol Optical Depth (AOD) reconstruction that defines the volcanic forcing time-series in ModelE2-R (Figure 1). This estimate is derived from sulfate peaks in ice cores, which are relatively well dated and referenced to the historical record during the satellite era. Crowley and Unterman (2013) provide an AOD history over 4 latitude bands (from 0-30° and 30-90° in both hemispheres). ModelE2-R uses a cubic spline to interpolate this forcing dataset over 24 latitude bands. The choice of volcanic eruptions used for the LM analysis (section 2.2 below) is based on the AOD dataset from this 24-latitude grid.

In addition to the model, we briefly explore post-L20 eruption results in the instrumental record. To do this, we take advantage of the NASA GISS Surface Temperature analysis (GISTEMP) land-ocean index (Hansen et al., 1999), and Global Precipitation Climatology Centre (GPCC) v6, a monthly precipitation dataset over land

396 (Schneider et al., 2011). For Figures 2 and 3 where ocean climatological data is shown,  
397 we use the Global Precipitation Climatology Project (GPCP) version 2.2 (Adler et al.,  
398 2003), a combined land station and satellite product available since 1979. These datasets  
399 are called upon to gauge the tropical climate response following the three L20 eruptions.  
400 We use the 2.5° resolution GPCC dataset, as that is comparable to the GISS model and  
401 what is justified by the station coverage in this part of the world. The GPCC product  
402 offers considerably better global and South American coverage than other precipitation  
403 datasets, although observational density for rainfall is still considerably more problematic  
404 over South America than for many other regions of the globe. There is a sharp drop-off in  
405 the number of rain gauge stations used earlier in the 20<sup>th</sup> century over much of the South  
406 American continent. Figure S1 shows the station density at the time of each L20 eruption,  
407 as well as the total number of land stations over South America with time.

408 Finally, in section 3.1 we present data from the Global Network of Isotopes in  
409 Precipitation (GNIP) accessible from the International Atomic Energy Agency (IAEA)  
410 for  $\delta^{18}\text{O}_p$ , as a test of the model's ability to track the seasonal hydrologic cycle in the  
411 form of its isotopic response over South America before discussing the Last Millennium  
412 results. Unfortunately, there is considerable spatial and temporal heterogeneity in the  
413 GNIP data over South America. In fact, only a few stations have data overlap with one or  
414 two eruptions and with a sufficient number of  $\delta^{18}\text{O}_p$  data points to establish reasonable  
415 seasonal or annual statistics. Additionally, the post-volcanic (L20) anomalous isotope  
416 field over South America strongly resembles the ENSO expression on the isotope field  
417 (Vuille et al., 2003a) and with large spread between events (not shown). This suggests  
418 that internal variability (ENSO) dominates the forced (volcanic) response in this very

small historical sample size, thereby leaving little hope that the prevailing network of observations is suitable for hypothesis testing and model validation in our context.

## 2.2 Super-posed Epoch and Composite Analysis

We present the spatial pattern of observed and simulated response for temperature and precipitation over land for two L20 eruptions (El Chichón and Mt. Pinatubo). Results are shown for annual-means in 1983 and 1992. We choose only two for brevity, as our argument that assessing the signal in any specific region is difficult in a small sample of eruptions is unaffected. Because of the dominant influence of unforced variability on tropical South American climate (Garreaud et al., 2009) overriding the volcanic signal during the L20 eruptions, we instead present a superposed epoch anomaly composite of the tropical-mean temperature anomaly, zonally averaged from 30°S to 30°N. Results are shown for years -3 to +5, with zero defining the time of the eruption. This composite is formed for all three L20 eruptions. In all cases, the five years prior to the eruption were subtracted from the superposed composite. Other sensible choices for the non-eruption reference period do not significantly change the results.

For the full LM spatial composites, we use only eruptions where vertically integrated (15 to 35 km) stratospheric AOD averaged from 30°N to 30°S exceeds 0.1 for at least 12 consecutive months in the simulation (top panel in Figure 1). For the LM composites, we focus only on seasonal (DJF and JJA) composites, and a given season will enter the composite if at least 2/3 months meet the AOD threshold; this criterion yields 15 eruptions since 850 C.E. The selection of events used in the LM composite is

442 very weakly sensitive to this choice of latitude band. Mt. Pinatubo is the only L20  
443 eruption in this composite, and is actually one of the smallest eruptions in this selection  
444 based on the maximum AOD encountered near the time of the eruption (see Table 1 for  
445 dates of each event). We believe sampling a larger number of events with greater forcing  
446 is a better way to understand the volcanic response in this model, rather than increasing  
447 the ensemble size for the L20 events. We do stress, however, that there is considerable  
448 forcing uncertainty during the LM and so the model results ought to be viewed as a slave  
449 to the imposed AOD and particle size distribution.

450 For the LM “non-eruption” fields, we use 15 years prior to the eruption as a  
451 reference period to calculate the anomaly for each event, unless another event occurs  
452 during that time (overlap occurs only once for eruptions in 1809 and 1815) in which case  
453 the pre-1809 climatology is used twice. The exception is for Mt. Pinatubo, which again  
454 uses the previous five years to calculate the anomaly. When constructing seasonal  
455 averages of  $\delta^{18}\text{O}_p$ , the oxygen isotope value for each month is weighted by the  
456 precipitation amount during that month, at each grid cell.

457 Since each post-eruption difference field is computed using the immediate  
458 response minus a local 15-year climatology, time is not relevant in this analysis and so  
459 we use all three members with the Crowley forcing (representing over 3,000 years of  
460 simulation time) to generate a composite that features 45 volcanic “events” (15 eruptions  
461 in each of the three members). In the historical (post-1850) extension of these runs, the  
462 coding error that resulted in a mis-implementation of the Gao forcing is not an issue, and  
463 so we use six ensemble members each (three volcanic events in six ensemble members)  
464 for the L20 results.

465       The ensemble-mean composite results displayed for the LM eruptions include  
466 contributions from three members that differ not just in the internal variability, but also in  
467 their solar and land-use forcing. Similarly, the L20 results are from model runs that also  
468 include other transient historical forcings occurring at the time of the eruption, including  
469 greenhouse gas increases throughout the duration of the event (although these forcings  
470 are the same among all ensemble members). However, in all cases we focus only on the  
471 immediate years after the eruption. Since the primary signal of interests is expected to be  
472 large compared to the impact of more slowly varying and smaller-amplitude forcings, the  
473 ensemble spread for a given eruption can be interpreted as a sampling of the model  
474 internal variability coincident with the event. We have tested our composite results using  
475 the same dates as our volcanic events in simulations with other varying forcings but with  
476 no volcanoes (there are no volcano-only runs with this model version for the LM), and  
477 the results are indistinguishable from noise (not shown). The LM composite results are  
478 discussed in section 3.2.

479       Finally, it is now well appreciated that any climate response under investigation  
480 will be shackled to the spatial structure of the forcing imposed on a model. For example,  
481 preferential heating/cooling of one hemisphere will induce different tropical precipitation  
482 responses than a well-mixed gas that behaves CO<sub>2</sub>-like (Kang et al., 2008, 2009; Frierson  
483 and Hwang, 2012; Haywood et al., 2012). Figures S2 and S3 show the latitudinal AOD  
484 distribution structure for all eruptions used in the generation of the LM composites within  
485 ModelE2-R. The mean of all events is rather symmetric between hemispheres (though  
486 somewhat skewed toward the Southern Hemisphere tropics), and similar to the pattern  
487 expected with CO<sub>2</sub> change, the forcing is largest in the tropics. Thus, the resulting climate

responses outlined in this paper ought to be viewed as a response consistent with a forcing that is relatively symmetric about the equator. Results from volcanic eruptions with emphasis on the spatial structure of forcing will be reported in a separate paper.

### 2.3. Influence of ENSO on the Late 20<sup>th</sup> Century (L20) eruptions

For the L20 volcanic events, El Niño events are occurring quasi-simultaneously with the eruption. This introduces a pervasive issue when attempting to isolate the volcanic signal (e.g., Robock, 2003; Trenberth and Dai, 2007; Joseph and Zeng, 2011) and is particularly important over South America (e.g. Garreaud et al., 2009).

In order to remove the effects of ENSO from the super-posed epoch and spatial composite analyses described above in the GISTEMP and GPCC data, we first perform a multiple regression with the variable of interest over the period 1951-2005 using a linear time trend and the Niño 3 index as predictors (5°N-5°S, 150°W -90°W, data from <http://www.cpc.ncep.noaa.gov/data/indices/>) over the same period, excluding two years of data after each L20 eruption. At each grid cell, the Niño 3 index is lagged from 0-6 months and the correlation coefficient with the maximum absolute value (since a positive index can induce a negative anomaly in the variable of interest) is found. This is similar to the approach used in Joseph and Zeng (2011), allowing the maximum ENSO influence to be removed at each grid point at the expense of contemporaneous relationships. The lagged Niño index is then regressed against the time series of each variable and the residual from this regression is retained. This approach assumes a linear relationship between ENSO and the climate response over South America, an assumption that appears

justified on inter-annual to decadal time scales (Garreaud et al., 2009).

For each of the six ensemble members used in the model L20 composite, a similar procedure is performed in which the Niño 3 index (consistent with the realization of the Niño 3 domain SSTs in that model simulation) is calculated and regressed out in the same manner. For the full LM computations, the number of larger-amplitude events in the three-ensemble member composite should help average out the influence of Pacific SST variability, and no ENSO removal procedure is applied.

### 3. Results and Discussion

#### 3.1. L20

Figure 3 illustrates that ModelE2-R reproduces the seasonal cycle of climatological rainfall (comparing Figure 3a with 3b) and oxygen isotope distribution (comparing Figure 3c with 3d) with some fidelity over South America. This includes a meridional migration of the ITCZ toward the summer hemisphere and an intensification of the South American monsoon during DJF. Where data permit (Figure 3c) there is good agreement between model and observations, both displaying oxygen isotope DJF enrichment relative to JJA in the tropics north of the equator and the higher latitudes south of 30°S, and depletion in the continental interior south of the equator associated with the monsoon wet season. ModelE2-R (Figure 3b) tends to produce too much precipitation over northeastern Brazil although the gross features of the seasonal migration in rainfall are well captured. This ability to accurately simulate the seasonality

of  $\delta^{18}\text{O}_p$  over the tropical Americas has also been noted in two atmospheric GCMs with no coupled ocean (NASA-GISS II and ECHAM-4, see Vuille et al., 2003a).

Figure 4 shows the ENSO-removed super-posed epoch analysis for tropical temperature associated with the recent three L20 eruptions. There is good agreement between the observed and modeled temperature response, both in amplitude and recovery timescale. The tropical-mean cooling is on the order of several tenths of a degree, and larger after Mt. Pinatubo (not shown individually).

The spatial structure of the post- El Chichón and Pinatubo events in land observations and the individual model realizations are shown in Figures 5 and 6, respectively. Observations exhibit cooling over much of the globe, especially after Mt. Pinatubo that is largely reproduced by the model. However, there is considerable spread among the individual ensemble members and between the two events, indicating a large role for internal variability in dictating the observed spatial pattern following these events. This is also true over South America.

In GISTEMP, the high-latitudes of South America cool more than the tropical region of the continent after Mt. Pinatubo. There is still a residual signal from ENSO in tropical South America following both L20 eruptions that is not reproduced by the model. This is not unexpected, since ENSO events comparable to the magnitude of the historic realizations due not occur coincident with the volcanic forcing in the individual ensemble members. The magnitude of this signal is sensitive to the Niño index used in the regression method described above. Without ENSO removal, tropical South America warms following the two eruptions (not shown). The influence of ENSO appears minimal over the higher latitude sectors of the continent.

The precipitation pattern following the L20 eruptions exhibits substantial variability in space and across eruptions, with a general drying pattern over land in tropical latitudes. South America experiences less precipitation near the equator after Mt. Pinatubo (see also Trenberth and Dai, 2007), a pattern reproduced in some of the ensemble realizations.

It should be noted that model-observation comparison is hindered not just by internal variability, but also by the specified historical volcanic forcing in the model. In fact, the Stratospheric Aerosol and Gas Experiment (or SAGE) II satellite sensor was saturated by the aerosol cloud after Mt. Pinatubo; subsequent work (Santer et al., 2014; Schmidt et al., 2014c) suggests that the forcing following Pinatubo is too large in the CMIP5 generation of models. It is likely that CMIP6/PMIP4 will feature a reduced AOD and different particle size.

Because of the considerable variability seen in observations (following historical eruptions) and also across ensemble members, it is evident that a larger signal-to-noise ratio than is available from the L20 eruptions alone is required to help isolate any volcanic signal. ModelE2-R is the laboratory from which we proceed to sample a larger number of events, some of which contain larger amplitude than the L20 eruptions.

## 3.2. Last Millennium Composites

### 3.2.1. Temperature and Precipitation

Figure 7 shows the LM post-volcanic temperature composite for all 45 events. During both seasons, cooling is statistically significant over virtually the entire continent (stippling indicates significance at the 90% level, t-test). The temperature response is strongest in the interior of the continent, particularly during the austral winter. The enhanced high-latitude cooling exhibited in the observations after Mt. Pinatubo does not emerge in the model composite.

The precipitation anomalies for the LM composite are shown in Figure 8. As expected, there is a distinct seasonal structure in the response, with the largest anomaly concentrated in a narrow region north of the equator during austral winter, coincident with the location of climatological rainfall maxima in the region. During JJA, precipitation increases in the North Atlantic region following volcanic eruptions, while very strong and statistically significant precipitation reductions occur just north of the equator (including over northern Brazil, Ecuador, Venezuela, Colombia, and Guyana) and encompassing the northern Amazon Basin. This signal is consistent with a weakening of the moisture flux owing to the decrease in saturation vapor pressure due to cooling that is demanded by Clausius-Clapeyron (Held and Soden, 2006). During this season, the precipitation response is significant virtually everywhere in northern South America. Supplementary Figure (S5) further illustrates that the JJA precipitation response is remarkably robust to all eruptions that enter into the composite.

Figure 9b illustrates the relationship between area-averaged precipitation from [20°S to 0°, 77.5°W to 45°W \(for DJF\)](#) and [0° to 10°N, 77.5°W to 52.5°W \(for JJA\)](#) and the maximum AOD encountered for each eruption. These two regions were selected to reflect the seasonal migration of rainfall ([Figure 2, 3](#)). 15 eruptions are displayed with the

602 | three-member ensemble spread given for each. Precipitation only increases north of the  
603 | equator during austral winter in a few model realizations. Moreover, the magnitude of the  
604 | precipitation response during JJA scales with the size of the eruption, particularly for  
605 | very large eruptions (e.g., comparing five eruptions with AOD > 0.3 vs. those with  
606 | smaller perturbations, although the spread amongst the ensemble members is large). The  
607 | spatial composite for each individual eruption (each averaged over the three ensemble  
608 | members) is shown in Figure S5.

609 |       The precipitation response during austral summer is more difficult to interpret  
610 | (Figure 8a). During this season, the zonally oriented Atlantic ITCZ migrates southward  
611 | and the SACZ becomes more intense as it is connected with the area of convection over  
612 | the central and southeastern part of the continent. It is noteworthy that the land cools  
613 | substantially more than the surrounding ocean (Figure 7), which one could expect to  
614 | weaken the monsoon-sourced precipitation during DJF. While precipitation is indeed  
615 | reduced over the tropical continent, the response is weaker than in JJA and less spatially  
616 | coherent, with many areas failing to meet statistical significance. An analysis of the  
617 | individual responses reveals that the signal is more eruption-dependent during DJF than  
618 | during JJA (see Figure S4), with a few events actually exhibiting modest increases in  
619 | precipitation. Nonetheless, there is a clear tendency for reduced DJF precipitation within  
620 | the SAMS region, although there is little to no dependence of the mean rainfall anomaly  
621 | on the magnitude of the AOD perturbation, at least above the 0.1 threshold used in this  
622 | study (Figure 9b), unlike for equatorial South America during JJA. Conversely, the  
623 | temperature response (Figure 9a) depends on the size of the eruption in both seasons, as  
624 | is expected.

Chris Colose 2/17/2016 8:58 PM

**Deleted:** All data is zonally averaged from 75°W to 45°W.

### 3.2.2. Tropical Hydroclimate Response

Since the South American climate is intimately linked to large-scale tropical dynamics, the global precipitation composite is shown in Figure S6 to better inform the model response. The most robust signal is characterized by a reduction in tropically averaged precipitation and the tendency for wet regions to become drier, and dry regions to become wetter (see also Iles et al., 2013; [Iles and Hegerl, 2014](#)), in contrast to the anticipated hydrologic response in a future, higher-CO<sub>2</sub> world (Held and Soden, 2006).

This pattern is a thermodynamic effect linked to reduced moisture convergence within the convergence zones and to reduced moisture divergence in the descending zones of the Hadley cell, which reduces the contrast in values of precipitation minus evaporation (P-E) between moisture convergence and divergence regions (Chou et al., 2009). The complete hydrologic response of the  $\Delta P$ -E field (not shown) has the same spatial structure as the  $\Delta P$  field, since evaporation is decreasing nearly everywhere in the tropics. Because both P and E are decreasing on the equator-ward flank of the ITCZ the  $\Delta P$ -E signal is rather weak in the deep tropics, while  $\Delta P$ -E increases more rapidly than  $\Delta P$  in the subtropics.

The tendency for modest precipitation anomalies over the continent during DJF appears to be part of a pattern that spans a broad swath of longitudes across the entire deep tropics in association with the seasonal cycle. Nonetheless, the response during DJF is weaker over land.

### 3.2.3. Oxygen Isotope Anomalies

In order to relate the responses discussed in the previous sections back to a potentially observable paleoclimate metric, we show the composite  $\Delta\delta^{18}\text{O}_p$  field for the DJF and JJA seasons in South America (Figure 10). It should be cautioned that much of the isotopic variability that can be observed in proxies within the continental interior or high-elevation glacier sites will likely be seasonally biased toward the wet season months (Hardy et al., 2003).

During the JJA season, there is a strong enrichment of the  $\delta^{18}\text{O}_p$  pattern that is zonally extended over equatorial South America. In addition, there is a corresponding  $\delta^{18}\text{O}_p$  depletion in the adjacent North Atlantic sector. This response is inextricably coincident with the strong change in precipitation in the ITCZ domain that was assessed in Figure 8, and is broadly consistent with a “rainfall amount” control on the isotopic imprint (Dansgaard, 1964). South of approximately 15°S, the sign of the anomaly reverses to a depletion of the heavy isotope.

During the austral summer, volcanic eruptions lead to a clear negative excursion in  $\delta^{18}\text{O}_p$  over virtually the entire SAMS region, including the Amazon basin, tropical Andes, and eastern Brazil. The statistical significance of the resulting isotopic anomaly extends throughout most of the landmass within the tropics and in the North Atlantic. There are small but non-significant exceptions (positive  $\delta^{18}\text{O}_p$  excursions) such as in eastern Brazil. The negative excursions also include regions outside of the SAMS belt in the subtropics and mid-high latitudes of South America.

672 The austral summer  $\delta^{18}\text{O}_p$  depletion is the opposite sign from what one would  
673 expect if the reduced precipitation were driving the isotopic response. Thus, it may well  
674 be that the strong temperature response to volcanic eruptions dominates the continent-  
675 wide oxygen isotope depletion during the DJF season and in the extratropics during JJA  
676 over the relatively weak precipitation response. Precipitation on the other hand appears to  
677 be the primary control knob of  $\Delta\delta^{18}\text{O}_p$  during JJA within the ITCZ region.

678 The correlation between  $\Delta\delta^{18}\text{O}_p$  and temperature or precipitation, [based on a](#)  
679 [regression using all 45 volcanic events, is](#) reported in Figure 9, using the same domains  
680 for DJF and JJA described in section 3.2.1. In the case of volcanic forcing it appears that  
681 the amplitude of the temperature response to volcanic eruptions over tropical South  
682 America is [larger than the rather weak and spatially incoherent precipitation signal,](#)  
683 [although both the temperature and precipitation coefficients must be considered to](#)  
684 [characterize the isotopic variability during this season \(Figure S7\).](#) This may explain why  
685 the DJF isotopic signal related to volcanic eruptions seems to respond to atmospheric  
686 cooling, even in the tropics, where isotopic variability is usually more closely associated  
687 with changes in the hydrologic cycle. During JJA, the isotopic enrichment is much more  
688 [closely](#) associated with precipitation reduction north of the equator, [whereas the JJA](#)  
689  [\$\Delta\delta^{18}\text{O}\_p\$ -temperature relationship is weak and non-significant.](#)

690 Taken together, these results suggest that the primary controls on oxygen isotope  
691 variability are forcing and event-dependent, rather than being determined inherently by  
692 the latitude of interest (e.g., “precipitation driven” in the tropics and “temperature driven”  
693 in the extratropics). This conclusion is compelled by the fact that the precipitation  
694 production and distribution in proxy records are the result of an interaction between

Chris Colose 2/19/2016 7:01 PM

Deleted: are

Chris Colose 2/17/2016 11:12 PM

Deleted: -

Chris Colose 2/17/2016 11:12 PM

Deleted: much

698 multiple scales of motion in the atmosphere, the temperature of air in which the  
699 condensate was embedded, and exchange processes operating from source to sink of the  
700 parcel deposited at a site. Thus, a consistent description of how to interpret oxygen  
701 isotopes into a useful climate signal cannot be given without considering all of these  
702 processes and the target process of interest.

703 To further complement the spatial analysis, a composite Hovmöller diagram is  
704 utilized (Figure 11) in order to illustrate the time-evolution of the temperature,  
705 precipitation, and oxygen isotope response. For this plot, the start of each eruption is  
706 defined as the closest January to the first month in which AOD reaches 0.1 in order to  
707 illustrate the seasonal evolution (rather than compositing by “month from each eruption”  
708 as in Figure 3). Therefore, for all 45 events in the composite, the local AOD may reach  
709 this threshold within five months (before or after) of the January baseline point (eruptions  
710 in June are rounded up to the following January). The Hovmöller composites are plotted  
711 for ten years (beginning January three years prior to the eruption). The closest January  
712 point to the start of each eruption occurs in the 37<sup>th</sup> month of the Hovmöller (solid black  
713 line in Figure 11a,b,d). Results are zonally averaged from [77.5°W to 45°W](#).

714 Figure 11a demonstrates a substantial temperature anomaly that peaks south of  
715 10°S (compare also to Figure 7). The cooling lasts for several years following the  
716 eruption, and decays gradually until most of the signal is lost (~4 years after the eruption  
717 in the South American sector), but remains 0.1-0.2°C colder than the pre-eruption  
718 climatology. The zonally averaged peak reductions in South American precipitation  
719 anomalies occur over the tropical latitudes and last for a comparable period of time as the  
720 maximum temperature response. The precipitation anomaly itself migrates synchronously

Chris Colose 2/19/2016 6:33 PM

**Deleted:** , across the SAMS region.

with the seasonal cycle (red line in Figure 11c maps out the latitude of maximum climatological precipitation averaged over all 15 year climatologies of each 45-member event, as a function of time of year). Figure 11b indicates that the largest precipitation response is confined to the equatorial and northern regions during JJA, with weak protrusion into higher tropical latitudes only 1-2 years after the eruption. The JJA isotopic enrichment in northern South America lasts for two seasons in our composite, while there is sustained isotopic depletion during DJF in the SASM region for about three years (Figure 11d)

Figure 12 provides additional statistical insight into the magnitude of the excursions described in this section. Here, we sampled 100 random 45-event composites in a control simulation with no external forcing (each “event”, two seasons in length, is defined as an anomaly expressed relative to a pre-eruption climatology as done previously). The anomalies were averaged over the same areas as in Figure 9, with different domains for DJF and JJA. Notably, for both seasons and for all three variables examined, the single 45-event post-volcanic composite (purple square) lies outside the distribution of all sampled 45-event composites constructed with no external forcing. Nonetheless, the distribution for a smaller sample of events (black circles denote the data for each (15) eruption, each averaged over the three ensemble members) shows considerable spread.

The  $\delta^{18}\text{O}_p$  anomalies discussed above result from changes in the isotopic content of precipitation, which may be due to changes in precipitation amount or to other changes in the isotopic composition of the water vapor that condensed to form the precipitate. The changes are not determined by changes in the seasonality of the precipitation. To

illustrate this (Figure S8), we decomposed the  $\Delta\delta^{18}\text{O}_p$  field (see Liu and Battisti, 2015) by weighting the monthly oxygen isotope field by the pre-eruption precipitation values. The results are indistinguishable from the total  $\Delta\delta^{18}\text{O}_p$  field, suggesting that any changes in monsoon seasonality are negligible in contributing to the isotopic signal, unlike the orbital case considered in Liu and Battisti (2015).

#### 4. Conclusions

In this study, we have analyzed the response of temperature, precipitation, and  $\delta^{18}\text{O}_p$  over South America to volcanic forcing associated with large tropical eruptions during the Last Millennium. It is now well known that volcanic eruptions lead to large-scale cooling throughout the tropics, and this result extends to most of the South American continent as well, except in regions that may be simultaneously affected by opposing ENSO behavior. In general, the precipitation response has been more enigmatic, though our results are in broad agreement with numerous other studies showing that there is a substantial decline in tropical-mean precipitation.

However, the immediate post-volcanic impact over South America has a complex seasonal and spatial structure. During the austral winter, the precipitation response over the continent is slaved to the response of the large-scale circulation, including a weakening of rainfall intensity within the ITCZ that is migrating northward. In the extratropics, the continent cools and exhibits slight precipitation declines nearly everywhere. Our results suggest the seasonal monsoon precipitation (during DJF) in ModelE2-R exhibits a fairly weak response that is scattered across the continent. It

appears that volcanic forcing preconditions the tropical rainfall over the continent to decline during the wet season, but that this response is likely to be eruption-dependent and may be overwhelmed by internal variability.

A unique aspect of this study was to probe the  $\delta^{18}\text{O}_p$  response to volcanic eruptions. During JJA, isotopes become heavily enriched in northern South America as convective activity produces substantially less precipitation. No such relation was found during the monsoon season, even within the tropics, where the large cooling appears to lead to more depleted  $\delta^{18}\text{O}_p$ , despite a weakened hydrologic cycle and reduced monsoon precipitation. In the extratropics, it appears that the temperature decline is driving isotopes toward more depleted values.

Unfortunately validation of our model results is hindered by the paucity of observational stable isotope data and by the coincidence of volcanic eruptions with ENSO events over the 20<sup>th</sup> century. Nonetheless our results may provide some guidance in the search of volcanic signals in high-resolution isotopic proxy data from South America. Given the importance of volcanic forcing for climate variability over the past millennium, and in particular the LIA period, which has been identified as a period of significant climatic perturbation in isotopic proxies from South America, a better understanding of the climatic response to volcanic forcing over this region is urgently needed.

#### *Acknowledgments:*

This study was funded by NOAA C2D2 NA10OAR4310126 and NSF awards AGS-1003690 and AGS-1303828. We would like to thank NASA GISS for institutional

792 support, in addition to Raphael Neukom and an anonymous reviewer for the constructive  
793 comments that helped improve the manuscript. Computing resources supporting this  
794 work were provided by the NASA High-End Computing (HEC) Program through the  
795 NASA Center for Climate Simulation (NCCS) at Goddard Space Flight Center.  
796 GPCP/GPCC data provided by the NOAA/OAR/ESRL PSD, Boulder, Colorado, USA,  
797 from their Web site at <http://www.esrl.noaa.gov/psd/>.  
798

799 **References**

- 800 Adler, R.F., Huffman, G.J., Chang, A., Ferraro, R., Xie, P., Janowiak, J., Rudolf, B.,  
801 Schneider, U., Curtis, S., Bolvin, D., Gruber, A., Susskind, J., and Arkin, P.: The  
802 Version 2 Global Precipitation Climatology Project (GPCP) Monthly Precipitation  
803 Analysis (1979-Present), *J. Hydrometeor.*, 4, 1147-1167, 2003.
- 804 Apaestegui, J., Cruz, F.W., Sifeddine, A., Vuille, M., Espinoza, J.C., Guyot, J.L., Khodri,  
805 M., Strikis, N., Santos, R.V., Cheng, H., Edwards, L., Carvahlo E., and Santini, W.:  
806 Hydroclimate variability of the northwestern Amazon basin near the Andean foothills  
807 of Peru related to the South American Monsoon System during the last 1600 years,  
808 *Clim. Past*, 10, 1967-1981, 2014.
- 809 Anchukaitis, K.J., Buckley, B.M., Cook, E.R., Cook, B.I., D'Arrigo, R.D., and Ammann,  
810 C.M.: The influence of volcanic eruptions on the climate of the Asian monsoon  
811 region, *Geophys. Res. Lett.*, 37, L22703, 2010.
- 812 [Atwood, A.R., Wu, E., Frierson, D.M.W., Battisti D.S., and Sachs J.P.: Quantifying](#)  
813 [climate forcings and feedbacks over the last millennium in the CMIP5-PMIP3, \*J.\*](#)  
814 [Climate, 29, 1161-1178, 2016.](#)
- 815 Bird, B.W., Abbott, M.B., Rodbell, D.T., and Vuille M.: Holocene tropical South  
816 American hydroclimate revealed from a decadal resolved lake sediment  $\delta^{18}\text{O}$  record,  
817 *Earth Planet. Sci. Lett.*, 310, 192-202, 2011.
- 818 Bradley, R.S., Vuille, M., Hardy, D.R., and Thompson, L.G.: Low latitude ice cores  
819 record Pacific sea surface temperatures, *Geophys. Res. Lett.*, 30, 1174, 2003.

820 Chou, C., Neelin, J.D., Chen, C.A., and Tu, J.Y.: Evaluating the “Rich-Get-Richer”  
821 Mechanism in Tropical Precipitation Change under Global Warming, *J. Climate*, 22,  
822 1982–2005, 2009.

823 Coakley, J.A., and Grams, G.W.: Relative Influence of Visible and Infrared Optical  
824 Properties of a Stratospheric Aerosol Layer on the Global Climate, *J. Appl. Meteor.*,  
825 15, 679–691, 1976.

826 Cole-Dai, J.: Volcanoes and climate, *Wiley Interdisciplinary Reviews: Climate Change*,  
827 1, 824-839, 2010.

828 Crowley, T.J.: Causes of climate change over the past 1000 years, *Science*, 289, 270–  
829 277, 2000.

830 Crowley, T. J. and Unterman M.B.: Technical details concerning development of a  
831 1200-yr proxy index for global volcanism, *Earth Syst. Sci. Data*, 5, 187–197, 2013.

832 Cruz, F.W., Burns, S.J., Karmann, I., Sharp, W.D., Vuille, M., Cardoso, A.O., Ferrari,  
833 J.A., Dias, P.L.S., and Viana, O.: Insolation-driven changes in atmospheric  
834 circulation over the past 116,000 years in subtropical Brazil, *Nature*, 434, 63-66, 2005.

835 Dansgaard, W.: Stable isotopes in precipitation, *Tellus*, 16, 436–468, 1964.

836 D’Arrigo, R., Wilson, R., and Tudhope, A.: The impact of volcanic forcing on tropical  
837 temperatures during the past four centuries, *Nature Geosci.*, 2, 51–56, 2009.

838 da Silva, A. E. and de Carvalho, L. M. V.: Large-scale index for South America Monsoon  
839 (LISAM), *Atmos. Sci. Lett.*, 8, 51–57, 2007.

840 Driscoll, S., Bozzo, A., Gray, L.J., Robock, A., and Stenchikov G.: Coupled Model  
841 Intercomparison Project 5 (CMIP5) simulations of climate following volcanic  
842 eruptions, *J. Geophys. Res.*, 117, D17105, 2012.

843 Emile-Geay, J., Seager R., Cane, M.A., Cook, E.R., and Haug, G.H.: Volcanoes and  
844 ENSO over the Past Millennium, *J. Climate*, 21, 3134–3148, 2008.

845 Esper J., Schneider L., Krusic P.J., Luterbacher J., Büntgen U., Timonen M., Sirocko F.  
846 and Zorita E.: European summer temperature response to annually dated volcanic  
847 eruptions over the past nine centuries, *B. Volcanol.* 75, 1-14, 2013.

848 Evan, A.T.: Atlantic hurricane activity following two major volcanic eruptions, *J.*  
849 *Geophys. Res.*, 117, D06101, 2012.

850 Field, R.D., D. Kim, A.N. LeGrande, J. Worden, M. Kelley, and G.A. Schmidt:  
851 Evaluating climate model performance in the tropics with retrievals of water isotopic  
852 composition from Aura TES, *Geophys. Res. Lett.*, 41, 16, 6030-6036, 2014.

853 Fischer, E.M., Luterbacher, J., Zorita, E., Tett, S.F.B., Casty, C., and Wanner, H.:  
854 European climate response to tropical volcanic eruptions over the last half  
855 millennium, *Geophys. Res. Lett.*, 34, L05707, 2007.

856 Frierson, D.M.W., and Hwang Y.: Extratropical Influence on ITCZ Shifts in Slab Ocean  
857 Simulations of Global Warming, *J. Climate*, 25, 720–733, 2012.

858 Gao, C., Robock, A., and Ammann, C.: Volcanic forcing of climate over the past 1500  
859 years: an improved ice core-based index for climate models, *J. Geophys. Res.*, 113,  
860 D23111, 2008.

861 Garreaud, R.D., Vuille, M., Compagnucci, R., and Marengo, J.: Present-day South  
862 American climate, *Palaeogeogr. Palaeoclimatol. Palaeoecol.*, 281, 180-195, 2009.

863 Gillett, N.P., Weaver, A.J., Zwiers, F.W., and Wehner, M.F.: Detection of volcanic  
864 influence on global precipitation, *Geophys. Res. Lett.*, 31, L12217, 2004.

865 Gillett, N.P., and Fyfe, J.C.: Annular mode changes in the CMIP5 simulations, *Geophys.*  
 866 *Res. Lett.*, 40, 1189–1193, 2013.  
 867 Gonzalez, P.L.M., Polvani, L.M., Seager, R., and Correa, G.J.P.: Stratospheric ozone  
 868 depletion: a key driver of recent precipitation trends in South Eastern South America,  
 869 *Climate Dyn.*, 42, 1-18, 2013.  
 870 Goosse, H., Crowley, T., Zorita, E., Ammann, C., Renssen, H., and Driesschaert, E.:  
 871 Modelling the climate of the last millennium: what causes the differences between  
 872 simulations? *Geophys. Res. Lett.*, 32, L06710, doi:10.1029/2005GL22368, 2005.  
 873 Hansen, J., Lacis A., Ruedy, R., and Sato, M.: Potential climate impact of Mount  
 874 Pinatubo eruption, *Geophys. Res. Lett.*, 19, 215-218, 1992.  
 875 Hansen, J., Ruedy, R., Glascoe, J., and Sato, M.: GISS analysis of surface temperature  
 876 change, *J. Geophys. Res.*, 104, 30997-31022, 1999.  
 877 Hardy, D.R., Vuille, M., and Bradley, R.S.: Variability of snow accumulation and  
 878 isotopic composition on Nevado Sajama, Bolivia, *J. Geophys. Res.*, 108, 4693, 2003.  
 879 Harshvardhan, and R.D. Cess: Stratospheric aerosols: effect upon atmospheric  
 880 temperature and global climate, *Tellus*, 28, 1-10, 1976.  
 881 Haywood, J.M., Jones, A., Bellouin, N., and Stephenson, D.: Asymmetric forcing from  
 882 stratospheric aerosols impacts Sahelian rainfall, *Nature Climate Change*, 3, 660-665,  
 883 2013.  
 884 Hegerl, G.C., Crowley, T.J., Baum, S.K., Kim, K.Y., and Hyde, W.T.: Detection of  
 885 volcanic, solar and greenhouse gas signals in paleo-reconstructions of Northern  
 886 Hemispheric temperature, *Geophys. Res. Lett.*, 30, 1242, 2003.  
 887 Hegerl, G.C., Crowley, T.J., Hyde, W.T., and Frame, D.J.: Climate sensitivity

888 constrained by temperature reconstructions over the past seven centuries, *Nature*, 440,  
889 1029–1032, 2006.

890 Held, I.M., and Soden, B.J.: Robust Responses of the Hydrological Cycle to Global  
891 Warming, *J. Climate*, 19, 5686–5699, 2006.

892 Hoffmann, G., and Heimann, M.: Water isotope modeling in the Asian monsoon region,  
893 *Quat. Inter.*, 37, 115–128, 1997.

894 Iles, C.E., Hegerl, G.C., Schurer, A.P., and Zhang, X.: The effect of volcanic eruptions on  
895 global precipitation, *J. Geophys. Res. Atmos.*, 118, 8770–8786, 2013.

896 [Iles, C. E., and Hegerl G. C., The global precipitation response to volcanic eruptions in](#)  
897 [the CMIP5 models, \*Environ. Res. Lett.\*, 9, 104012, 2014.](#)

898 Joseph, R., and Zeng, N.: Seasonally Modulated Tropical Drought Induced by Volcanic  
899 Aerosol, *J. Climate*, 24, 2045–2060, 2011.

900 Kang, S.M., Held I.M., Frierson, D.M.W., and Zhao, M.: The Response of the ITCZ to  
901 Extratropical Thermal Forcing: Idealized Slab-Ocean Experiments with a GCM, *J.*  
902 *Climate*, 21, 3521–3532, 2008.

903 Kang, S.M., Frierson, D.M.W., and Held, I.M.: The Tropical Response to Extratropical  
904 Thermal Forcing in an Idealized GCM: The Importance of Radiative Feedbacks and  
905 Convective Parameterization, *J. Atmos. Sci.*, 66, 2812–2827, 2009.

906 Kang, S., Polvani, L., Fyfe, J., and Sigmond, M.: Impact of polar ozone depletion on  
907 subtropical precipitation, *Science*, 332, 951–954, 2011.

908 Kang, S. M., Frierson, D. M., and Held, I. M.: The tropical response to extratropical  
909 thermal forcing in an idealized GCM: The importance of radiative feedbacks and  
910 convective parameterization, *J. Atmos. Sci.*, 66, 2812–2827, 2009.

911 Kanner, L. C., Burns, S. J., Cheng, H., and Edwards, R. L.: High-latitude forcing of the  
 912 South American summer monsoon during the last glacial, *Science*, 335, 570–573,  
 913 2012.

914 Kanner, L. C., Burns, S. J., Cheng, H., Edwards, R. L., and Vuille, M.: High-resolution  
 915 variability of the South American summer monsoon over the last seven millennia:  
 916 insights from a speleothem record from the central Peruvian Andes, *Quat. Sci. Rev.*,  
 917 75, 1–10, 2013.

918 Kaplan, J. O., Krumhardt, K. M., Ellis, E. C., Ruddiman, W. F., Lemmen, C., and  
 919 Goldewijk, K. K.: Holocene carbon emissions as a result of anthropogenic land cover  
 920 change, *The Holocene*, 21, 775–791, doi:10.1177/0959683610386983, 2011.

921 Karpechko, A. Y., Gillett, N. P., Dall’Amico, M., and Gray, L. J.: Southern Hemisphere  
 922 atmospheric circulation response to the El Chichón and Pinatubo eruptions in coupled  
 923 climate models, *Q.J.R. Meteorol. Soc.*, 136, 1813–1822, 2010.

924 Krivova, N., Balmaceda, L., and Solanki, S.: Reconstruction of solar total irradiance  
 925 since 1700 from the surface magnetic flux, *Astron. Astrophys.*, 467, 335–346, 2007.

926 Lacis, A., Hansen, J., and Sato, M.: Climate forcing by stratospheric aerosols, *Geophys.*  
 927 *Res. Lett.*, 19, 1607–1610, 1992.

928 Ledru, M.-P., Jomelli, V., Samaniego, P., Vuille, M., Hidalgo, S., Herrera, M., and Ceron,  
 929 C.: The Medieval climate anomaly and the Little Ice Age in the eastern Ecuadorian  
 930 Andes, *Clim. Past*, 9, 307–321, 2013.

931 LeGrande, A.N., and Schmidt, G.A.: Ensemble, water-isotope enabled, coupled general  
 932 circulation modeling insights into the 8.2-kyr event, *Paleoceanography*, 23, PA3207,  
 933 2008.

934 LeGrande, A.N., and Schmidt, G.A.: Sources of Holocene variability of oxygen isotopes  
 935 in paleoclimate archives, *Clim. Past*, 5, 441-455, 2009.

936 Lewis, S.C., LeGrande A.N., Kelley, M., and Schmidt, G.A.: Modeling insights into  
 937 deuterium excess as an indicator of water vapor source conditions, *J. Geophys. Res.*  
 938 *Atmos.*, 118, 2, 243-262, 2013.

939 Lewis, S.C., LeGrande, A.N., Schmidt, G.A., and Kelley, M.: Comparison of forced  
 940 ENSO-like hydrological expressions in simulations of the pre-industrial and mid-  
 941 Holocene, *J. Geophys. Res. Atmos.*, 119, 12, 7064-7082, 2014.

942 Lewis, S.C., LeGrande, A.N., Kelley, M., and Schmidt, G.A.: Water vapour source  
 943 impacts on oxygen isotope variability in tropical precipitation during Heinrich events,  
 944 *Clim. Past*, 6, 325-343, 2010.

945 Liu, X. and Battisti, D.S.: The Influence of Orbital Forcing of Tropical Insolation on the  
 946 Climate and Isotopic Composition of Precipitation in South America, *J. Climate*, 28 ,  
 947 4841-4862, 2015.

948 Lucht, W., Prentice, I. C., Myneni, R. B., Sitch, S., Friedlingstein, P., Cramer, W.,  
 949 Bousquet, P., Buermann, W., and Smith, B.: Climatic control of the high-latitude  
 950 vegetation greening trend and Pinatubo effect, *Science*, 296, 1687–1689, 2002.

951 Ludlow, F., Stine, A. R., Leahy, P., Murphy, E., Mayewski, P. A., Taylor, D., Killen, J.,  
 952 Baillie, M. G., Hennessy, M., and Kiely, G.: Medieval Irish chronicles reveal  
 953 persistent volcanic forcing of severe winter cold events, 431–1649 CE,  
 954 *Environmental Research Letters*, 8, 024 035, 2013.

955 Man, W., Zhou, T., and Jungclaus, J. H.: Effects of large volcanic eruptions on global  
 956 summer climate and East Asian monsoon changes during the last millennium:  
 957 Analysis of MPI-ESM simulations, *J. Climate*, 27, 7394–7409, 2014.  
 958 Mann, M. E., Cane, M. A., Zebiak, S. E., and Clement, A.: Volcanic and solar forcing of  
 959 the tropical Pacific over the past 1000 years, *J. Climate*, 18, 447–456, 2005.  
 960 Marengo, J., Liebmann, B., Grimm, A., Misra, V., Silva Dias, P., Cavalcanti, I., Carvalho,  
 961 L., Berbery, E., Ambrizzi, T., Vera, C. S., Saulo, A. C., Nogues-Paegle, J., Zipser, E.,  
 962 Seth, A., and Alves, L. M.: Recent developments on the South American monsoon  
 963 system, *Int. J. Climatol.*, 32, 1–21, 2012.  
 964 Marengo, J. A., Liebmann, B., Kousky, V. E., Filizola, N. P., and Wainer, I. C.: Onset  
 965 and end of the rainy season in the Brazilian Amazon Basin, *J. Climate*, 14, 833–852,  
 966 2001.  
 967 McGregor, H. V., M. N. Evans, H. Goosse, G. Leduc, B. Martrat, J. A. Addison, P. G.  
 968 Mortyn, D. W. Oppo, M.-S. Seidenkrantz, M.-A. Sicre, S. J. Phipps, K. Selveraj, K.  
 969 Thirumalai, H. L. Filipsson and V. Ersek: Robust global ocean cooling trend for the  
 970 pre-industrial Common Era, *Nat. Geosci.*, 8, 671–677, 2015.  
 971 Miller, G. H., Geirsdóttir, Á., Zhong, Y., Larsen, D. J., Otto-Bliesner, B. L., Holland, M.  
 972 M., Bailey, D. A., Refsnider, K. A., Lehman, S. J., Southon, J. R., Anderson, C.,  
 973 Bjornsson, H., and Thordarson, T. Anderson, C., Bjornsson, H., and Thordarson, T.:  
 974 Abrupt onset of the Little Ice Age triggered by volcanism and sustained by sea-  
 975 ice/ocean feedbacks, *Geophys. Res. Lett.*, 39, 2012.  
 976 Miller, R.L., Schmidt, G.A., Nazarenko, L.S., Tausnev, N., Bauer, S.E., Del Genio, A.D.,  
 977 Kelley, M., Lo, K.K., Ruedy, R., Shindell, D.T., Aleinov, I., Bauer, M., Bleck, R.,

978 Canuto, V., Chen, Y.-H., Cheng, Y., Clune, T.L., Faluvegi, G., Hansen, J.E., Healy,  
 979 R.J., Kiang, N.Y., Koch, D., Lacis, A.A., LeGrande, A.N., Lerner, J., Menon, S.,  
 980 Oinas, V., Pérez García-Pando C., Perlwitz, J.P., Puma, M.J., Rind, D., Romanou, A.,  
 981 Russell, G.L., Sato, M., Sun, S., Tsigaridis, K., Unger, N., Voulgarakis, A., Yao, M.-  
 982 S., and Zhang, J.: CMIP5 historical simulations (1850-2012) with GISS ModelE2, J.  
 983 Adv. Model. Earth Syst., 6, 2, 441-477, 2014.

984 Minnis, P., Harrison, E., Stowe, L., Gibson, G., Denn, F., Doelling, D., and Smith, W.:  
 985 Radiative climate forcing by the Mount Pinatubo eruption, Science, 259, 1411–  
 986 1415, 1993.

987 Neukom, R. and Gergis, J.: Southern Hemisphere high-resolution palaeoclimate records  
 988 of the last 2000 years, The Holocene, 22, 501–524, 2012.

989 Nogués-Paegle, J. and Mo, K. C.: Alternating wet and dry conditions over South America  
 990 during summer, Monthly Weather Review, 125, 279–291, 1997.

991 Nogués-Paegle, J., Mechoso, C. R., Fu, R., Berbery, E. H., Chao, W. C., Chen, T.-C.,  
 992 Cook, K., Diaz, A. F., Enfield, D., Ferreira, R., Grimm A, Kousky V, Liebmann, B,  
 993 Marengo, J, Mo, K, Neelin, JD, Paegle, J, Robertson, A, Seth, A, Vera ,C, Zhou, J .:  
 994 Progress in Pan American CLIVAR research: understanding the South American  
 995 monsoon, Meteorológica, 27, 1–30, 2002.

996 Novello, V. F., Cruz, F. W., Karmann, I., Burns, S. J., Strikis, N. M., Vuille, M., Cheng,  
 997 H., Lawrence Edwards, R., Santos, R. V., Frigo, E., and Barreto E.A.S.:  
 998 Multidecadal climate variability in Brazil's Nordeste during the last 3000 years  
 999 based on speleothem isotope records, Geophys. Res. Lett., 39, 2012.

1000 Oman, L., Robock, A., Stenchikov, G., Schmidt, G. A., and Ruedy, R.: Climatic response  
 1001 to high-latitude volcanic eruptions, *J. Geophys. Res. Atmos.*, 110, 2005.  
 1002 Oman, L., Robock, A., Stenchikov, G. L., and Thordarson, T.: High-latitude eruptions  
 1003 cast shadow over the African monsoon and the flow of the Nile, *Geophys. Res.*  
 1004 *Lett.*, 33, 2006.  
 1005 Peng, Y., Shen, C., Wang, W.-C., and Xu, Y.: Response of summer precipitation over  
 1006 Eastern China to large volcanic eruptions, *J. Climate*, 23, 818–824, 2010.  
 1007 Pollack, J. B., Toon, O. B., Sagan, C., Summers, A., Baldwin, B., and Van Camp, W.:  
 1008 Volcanic explosions and climatic change: A theoretical assessment, *J. Geophys.*  
 1009 *Res.*, 81, 1071–1083, 1976.  
 1010 Pollack, J. B., Toon, O. B., and Wiedman, D.: Radiative properties of the background  
 1011 stratospheric aerosols and implications for perturbed conditions, *Geophys. Res.*  
 1012 *Lett.*, 8, 26–28, 1981.  
 1013 Pongratz, J., Reick, C., Raddatz, T., and Claussen, M.: A global land cover reconstruction  
 1014 AD 800 to 1992: Technical description, Max Planck Institute for Meteorology Rep.  
 1015 on Earth System Science 51, 72 pp., 2008.  
 1016 Robock, A.: Volcanic eruptions and climate, *Reviews of Geophysics*, 38, 191–219, 2000.  
 1017 Robock, A.: Volcanoes: Role in climate, *Encyclopedia of atmospheric sciences*, 10,  
 1018 2494–2500, 2003.  
 1019 Robock, A. and Mao, J.: The volcanic signal in surface temperature observations, *J.*  
 1020 *Climate*, 8, 1086–1103, 1995.

1021 Robock, A., Adams, T., Moore, M., Oman, L., and Stenchikov, G.: Southern Hemisphere  
 1022 atmospheric circulation effects of the 1991 Mount Pinatubo eruption, *Geophys. Res.*  
 1023 *Lett.*, 34, 2007.  
 1024 Russell, G. L., Miller, J. R., and Rind, D.: A coupled atmosphere-ocean model for  
 1025 transient climate change studies, *Atmosphere-ocean*, 33, 683–730, 1995.  
 1026 Santer, B.D., Bonfils C., Painter J.F., Zelinka, M.D., Mears, C., Solomon, S., Schmidt,  
 1027 G.A., Fyfe, J.C., Cole, J.N.S., Nazarenko, L., Taylor, K.E., and Wentz, F.J.:  
 1028 Volcanic contribution to decadal changes in tropospheric temperature, *Nature*  
 1029 *Geosci.*, 7, 3, 185-189, 2014.  
 1030 Sato, M., Hansen, J. E., McCormick, M. P., and Pollack, J. B.: Stratospheric aerosol  
 1031 optical depths, 1850–1990, *J. Geophys. Res. Atmos.*, 98, 22 987–22 994, 1993.  
 1032 Schmidt, G. A., LeGrande, A. N., and Hoffmann, G.: Water isotope expressions of  
 1033 intrinsic and forced variability in a coupled ocean-atmosphere model, *J. Geophys.*  
 1034 *Res. Atmos.*, 112, 2007.  
 1035 Schmidt, G. A., Jungclaus, J. H., Ammann, C. M., Bard, E., Braconnot, P., Crowley, T. J.,  
 1036 Delaygue, G., Joos, F., Krivova, N. A., Muscheler, R., Otto-Bliesner, B. L.,  
 1037 Pongratz, J., Shindell, D. T., Solanki, S. K., Steinhilber, F., and Vieira, L. E. A.:  
 1038 Climate forcing reconstructions for use in PMIP simulations of the last millennium  
 1039 (v1.0), *Geosci. Model Dev.*, 4, 33–45, 2011.  
 1040 Schmidt, G. A., Jungclaus, J. H., Ammann, C. M., Bard, E., Braconnot, P., Crowley, T.  
 1041 J., Delaygue, G., Joos, F., Krivova, N.A., Muscheler, R., Otto-Bliesner, B. L.,  
 1042 Pongratz, J., Shindell, D. T., Solanki, S. K., Steinhilber, F., and Vieira, L. E. A.:

1043 Climate forcing reconstructions for use in PMIP simulations of the Last Millennium  
 1044 (v1.1), *Geosci. Model Dev.*, 5, 185–191, 2012.

1045 Schmidt, G. A., Kelley, M., Nazarenko, L., Ruedy, R., Russell, G. L., Aleinov, I., Bauer,  
 1046 M., Bauer, S., Bhat, M. K., Bleck, R., Canuto, V., Chen, Y., Cheng, Y., Clune, T.  
 1047 L., DelGenio, A., de Fainchtein, R., Faluvegi, G., Hansen, J. E., Healy, R. J.,  
 1048 Kiang, N. Y., Koch, D., Lacis, A. A., LeGrande, A. N., Lerner, J., Lo, K. K.,  
 1049 Matthews, E. E., Menon, S., Miller, R. L., Oinas, V., Oloso, A., Perlwitz, J., Puma,  
 1050 M. J., Putman, W. M., Rind, D., Romanou, A., Sato, M., Shindell, D. T., Sun, S.,  
 1051 Syed, R., Tausnev, N., Tsigaridis, K., Unger, N., Voulgarakis, A., Yao, M.-S., and  
 1052 Zhang, J.: Configuration and assessment of the GISS ModelE2 contributions to the  
 1053 CMIP5 archive, *J. Adv. Model. Earth Syst.*, 6, 141–184, 2014a.

1054 Schmidt, G. A., Annan, J. D., Bartlein, P. J., Cook, B. I., Guilyardi, E., Hargreaves, J. C.,  
 1055 Harrison, S. P., Kageyama, M., LeGrande, A. N., Konecky, B., Lovejoy, S., Mann,  
 1056 M. E., Masson-Delmotte, V., Risi, C., Thompson, D., Timmermann, A., Tremblay,  
 1057 L.-B., and Yiou, P.: Using palaeo-climate comparisons to constrain future  
 1058 projections in CMIP5, *Clim. Past*, 10, 221–250, 2014b.

1059 Schmidt, G.A., Shindell, D.T., and Tsigaridis, K.: Reconciling warming trends, *Nat.*  
 1060 *Geosci.*, 7, 158-160, 2014c.

1061 Schneider, U., Becker, A., Finger, P., Meyer-Christoffer, A., Rudolf, B., Ziese, M.: GPCC  
 1062 Full Data Reanalysis Version 6.0 at 2.5 °: Monthly Land-Surface Precipitation from  
 1063 Rain-Gauges built on GTS-based and Historic Data, doi:10.5676/  
 1064 10.5676/DWD\_GPCC/FD\_M\_V6\_250, 2011.

1065 Schurer, A. P., Tett, S. F., and Hegerl, G. C.: Small influence of solar variability on  
 1066 climate over the past millennium, *Nat. Geosci.*, 7, 104–108, 2014.  
 1067 Seth, A., Rojas, M., and Rauscher, S. A.: CMIP3 projected changes in the annual cycle of  
 1068 the South American Monsoon, *Climatic Change*, 98, 331–357, 2010.  
 1069 Shindell, D. T., Schmidt, G. A., Mann, M. E., and Faluvegi, G.: Dynamic winter climate  
 1070 response to large tropical volcanic eruptions since 1600, *J. Geophys. Res. Atmos.*,  
 1071 109, 2004.  
 1072 Steinhilber, F., Beer, J., and Fröhlich, C.: Total solar irradiance during the Holocene,  
 1073 *Geophys. Res. Lett.*, 36, 2009.  
 1074 Stenchikov, G. L., Kirchner, I., Robock, A., Graf, H.-F., Antuna, J. C., Grainger, R.,  
 1075 Lambert, A., and Thomason, L.: Radiative forcing from the 1991 Mount Pinatubo  
 1076 volcanic eruption, *J. Geophys. Res. Atmos.*, 103, 13 837–13 857, 1998.  
 1077 Stothers, R. B. and Rampino, M. R.: Historic volcanism, European dry fogs, and  
 1078 Greenland acid precipitation, 1500 BC to AD 1500, *Science*, 222, 411–413, 1983.  
 1079 Thompson, L. G., Mosley-Thompson, E., Davis, M. E., Lin, P.-N., Henderson, K. A.,  
 1080 Cole-Dai, J., Bolzan, J. F., and Liu, K.-B.: Late glacial stage and Holocene tropical  
 1081 ice core records from Huascaran, Peru, *Science*, 269, 46–50, 1995.  
 1082 Thompson, L. G., Davis, M., Mosley-Thompson, E., Sowers, T. A., Henderson, K. A.,  
 1083 Zagorodnov, V. S., Lin, P. N., Mikhalevko, V. N., Campen, R. K., Bolzan, J. F.,  
 1084 Cole-Dai, J., and Francou, B.: A 25 000-year tropical climate history from  
 1085 Bolivian ice cores, *Science*, 282, 1858–1864, 1998.

1086 Thompson, L. G., Mosley-Thompson, E., Brecher, H., Davis, M., León, B., Les, D., Lin,  
 1087 P.-N., Mashiotto, T., and Mountain, K.: Abrupt tropical climate change: Past and  
 1088 present, *Proc. Natl. Acad. Sci.*, 103, 10536–10543, 2006.  
 1089 Timmreck, C.: Modeling the climatic effects of large explosive volcanic eruptions, Wiley  
 1090 *Interdisciplinary Reviews: Climate Change*, 3, 545–564, 2012.  
 1091 Trenberth, K. E. and Dai, A.: Effects of Mount Pinatubo volcanic eruption on the  
 1092 hydrological cycle as an analog of geoengineering, *Geophys. Res. Lett.*, 34, 2007.  
 1093 Turco, R., Whitten, R., and Toon, O.: Stratospheric aerosols: Observation and theory,  
 1094 *Rev. Geophys.*, 20, 233–279, 1982.  
 1095 Van Breukelen, M., Vonhof, H., Hellstrom, J., Wester, W., and Kroon, D.: Fossil  
 1096 dripwater in stalagmites reveals Holocene temperature and rainfall variation in  
 1097 Amazonia, *Earth Planet. Sc. Lett.*, 275, 54–60, 2008.  
 1098 Vera, C., Higgins, W., Amador, J., Ambrizzi, T., Garreaud, R., Gochis, D., Gutzler, D.,  
 1099 Lettenmaier, D., Marengo, J., Mechoso, C. R., Nogues-Paegle, J., Silva Dias, P. L.,  
 1100 and Zhang, C.: Toward a unified view of the American monsoon systems, *J.*  
 1101 *Climate*, 19, 4977–5000, 2006.  
 1102 Vimeux, F., Gallaire, R., Bony, S., Hoffmann, G., and Chiang, J. C.: What are the climate  
 1103 controls on  $\delta D$  in precipitation in the Zongo Valley (Bolivia)? Implications for the  
 1104 Illimani ice core interpretation, *Earth Planet. Sc. Lett.*, 240, 205–220, 2005.  
 1105 Vimeux, F., Ginot, P., Schwikowski, M., Vuille, M., Hoffmann, G., Thompson, L. G.,  
 1106 and Schotterer, U.: Climate variability during the last 1000 years inferred from  
 1107 Andean ice cores: A review of methodology and recent results, *Palaeogeogr.*,  
 1108 *Palaeoclimatol.*, 281, 229–241, 2009.

1109 Vuille, M. and Werner, M.: Stable isotopes in precipitation recording South American  
 1110 summer monsoon and ENSO variability: observations and model results, *Clim.*  
 1111 *Dynam.*, 25, 401–413, 2005.

1112 Vuille, M., Bradley, R. S., Werner, M., Healy, R., and Keimig, F.: Modeling  $\delta^{18}\text{O}$  in  
 1113 precipitation over the tropical Americas: 1. Interannual variability and climatic  
 1114 controls, *J. Geophys. Res. Atmos.*, 108, 2003a.

1115 Vuille, M., Bradley, R.S., Healy, R., Werner, M., Hardy D. R., Thompson, L. G., Keimig,  
 1116 F.: Modeling  $\text{d}^{18}\text{O}$  in precipitation over the tropical Americas: 2. Simulation of the  
 1117 stable isotope signal in Andean ice cores, *J. Geophys. Res.*, 108, D6, 4175, 2003b.

1118 Vuille, M., Burns, S., Taylor, B., Cruz, F., Bird, B., Abbott, M., Kanner, L., Cheng, H.,  
 1119 and Novello, V.: A review of the South American monsoon history as recorded in  
 1120 stable isotopic proxies over the past two millennia, *Clim. Past*, 8, 1309–1321, 2012.

1121 Wilmes, S., Raible, C., and Stocker, T.: Climate variability of the mid-and high-latitudes  
 1122 of the Southern Hemisphere in ensemble simulations from 1500 to 2000 AD, *Clim.*  
 1123 *Past*, 8, 373–390, 2012.

1124 Yoshimori, M., Stocker, T. F., Raible, C. C., and Renold, M.: Externally forced and  
 1125 internal variability in ensemble climate simulations of the Maunder Minimum, *J.*  
 1126 *Climate*, 18, 4253–4270, 2005.

1127 Zhang, D., Blender, R., and Fraedrich, K.: Volcanoes and ENSO in millennium  
 1128 simulations: Global impacts and regional reconstructions in East Asia, *Theor. Appl.*  
 1129 *Climatol.*, 111, 437–454, 2013.

1130 Zhou, J. and Lau, K.: Does a monsoon climate exist over South America? *J. Climate*, 11,  
 1131 1020–1040, 1998.

1132 Table 1: Time of Eruptions and Global Aerosol Optical Depth (AOD) from Crowley and  
 1133 Unterman (2013). List of eruptions used in study.  
 1134

**Table 1.** List of LM and L20 Eruptions

| Start Date of Eruption <sup>a</sup> | Seasons in LM Composite |           | Max<br>AOD <sup>b</sup> |
|-------------------------------------|-------------------------|-----------|-------------------------|
|                                     | DJF <sup>c</sup>        | JJA       |                         |
| Jan 971                             | 972                     | 971-972   | 0.22                    |
| Jan 1193                            | 1194                    | 1193-1194 | 0.16                    |
| Jul 1228                            | 1229-1251               | 1229-1230 | 0.38                    |
| Oct 1257                            | 1258-1260               | 1258-1259 | 0.69                    |
| Jan 1286                            | 1287-1288               | 1286-1287 | 0.28                    |
| Jul 1455                            | 1456-1458               | 1456-1458 | 0.41                    |
| Jan 1600                            | 1601                    | 1600      | 0.17                    |
| Jan 1641                            | 1642                    | 1641-1642 | 0.24                    |
| May 1673                            | 1674                    | 1674      | 0.21                    |
| Apr 1694                            | 1695-1697               | 1694-1696 | 0.24                    |
| Jan 1809                            | 1810-1811               | 189-1810  | 0.30                    |
| May 1815                            | 1816-1818               | 1815-1817 | 0.47                    |
| May 1835                            | 1836                    | 1835-1836 | 0.24                    |
| Jan 1883                            | 1884                    | 1884      | 0.20                    |
| Apr 1963 <sup>d</sup>               |                         |           | 0.11                    |
| Apr 1982 <sup>d</sup>               |                         |           | 0.12                    |
| Jun 1991                            | 1992                    | 1992      | 0.18                    |

<sup>a</sup>Start of Eruption dates based on when they can be identified in the Crowley /Sato time-series averaged over the latitude band from 30°S to 30°N. May be slightly different than actual eruption date.  
<sup>b</sup>Maximum AOD over the 30°S to 30°N latitude band encountered in monthly time-series during the duration of each event.  
<sup>c</sup>December in year prior to listed date.  
<sup>d</sup>Mt. Agung and El Chichón included in L20 but not LM composites.

1135  
 1136  
 1137

## List of Figure Captions

**Figure. 1.** Aerosol Optical Depth (AOD) used to force the NASA GISS ModelE2-R over the Last Millennium and (bottom) zoomed in on the period 1950-1999 (Crowley+Sato) as discussed in text. AOD is the vertically integrated (15-35 km) and latitudinal average from 30°S to 30°N. Note difference in vertical scale between graphs. Orange dashed line marks the AOD threshold for defining a LM eruption in the present study. Eruption events defined in text must sustain the threshold AOD for at least one year, so not all events above the orange dashed line are used in the composites.

**Figure. 2.** (Top) Observed Climatological Precipitation for DJF (shading, in mm day<sup>-1</sup>). SAMS box is drawn over the domain from 20°S to 0°, 77.5°W to 45°W and used for Figure 9 and 12. Data from the GPCP product, long-term climatological rainfall derived from years 1981 - 2010. (Bottom) As above, except for JJA. Box from 0° to 10°N, 77.5°W to 52.5°W used in averaging for Figures 9 and 12.

**Figure. 3.** Seasonal cycle (DJF minus JJA) of precipitation in **a)** GPCP precipitation product, from data in Figure 2 **b)** in ModelE2-R **c)**  $\delta^{18}\text{O}_p$  in GNIP data **d)** and  $\delta^{18}\text{O}_p$  in ModelE2-R. GNIP data only shown for stations with at least 90 reported  $\delta^{18}\text{O}_p$  values at a given station from 1960-present, in addition to at least ten data values for each month: December, January, February, June, July, and August. Stations with seasonal differences of less than +/- 1.0 per mil are also omitted in panel (c).

**Figure. 4.** Composite tropical (30°S to 30°N) temperature response following the L20 volcanic eruptions. Fill colors denote observed monthly anomalies using GISTEMP, with 24-month running average shown as solid black line. ModelE2-R ensemble mean is shown as solid orange line and dashed grey lines indicate the six individual ensemble members. Anomalies are referenced to 5 years prior to eruptions (years -5 to 0). Dashed purple lines encompass the 5-95% interval for monthly tropical-mean temperature anomalies (relative to the previous five-year mean) in the GISTEMP product from 1950-present. The calculation of this range omits data two years after the L20 eruptions. The range is not symmetric about zero due to the tropical warming trend during this interval. All data are based on the ENSO-removal technique discussed in text.

**Figure 5.** Annual-mean temperature change (°C, ocean masked) for each L20 eruption (labeled on plot) in GISTEMP (top row) and each ModelE2-R ensemble member, as discussed in text. All plots use ENSO-removal procedure described in text.

**Figure. 6.** As in Figure 5, except for precipitation change (mm day<sup>-1</sup>).

**Figure. 7.** Last Millennium post-volcanic temperature composite (°C) averaged over all 45 events during **a)** DJF and **b)** JJA from GISS ModelE2-R using procedure described in text. Stippling highlights areas with anomalies significant at  $p < 0.1$ .

**Figure. 8.** Last Millennium post-volcanic precipitation composite ( $\text{mm day}^{-1}$ ) with all eruption events during **a)** DJF and **b)** JJA from GISS ModelE2-R using procedure described in text. Stippling highlights areas with anomalies significant at  $p < 0.1$ .

**Figure. 9. a)** Average temperature anomaly during DJF within the SAMS region (red,  $20^{\circ}\text{S}$  to  $0^{\circ}$ ,  $77.5^{\circ}\text{W}$  to  $45^{\circ}\text{W}$ ) and equatorial South America during JJA (blue,  $0^{\circ}$  to  $10^{\circ}\text{N}$ ,  $77.5^{\circ}\text{W}$  to  $52.5^{\circ}\text{W}$ ) plotted against the peak AOD for all 15 eruptions (each point averaged over three ensemble members with the three member spread shown as horizontal bars) and **b)** As in a), but for precipitation. Dashed horizontal lines indicate the 5-95% range for a two-season average of each variable relative to the previous 15 years (averaged over the same domain) in the entire control simulation with no external forcing. In both panels, the correlation coefficient and p-value are reported for a) temperature and b) precipitation vs.  $\Delta\delta^{18}\text{O}_p$  in each season and over the same domain. The regression uses all 45 volcanic events.

**Figure. 10.** Last Millennium post-volcanic oxygen isotope in precipitation ( $\Delta\delta^{18}\text{O}_p$ ) composite (per mil) with all eruption events during **a)** DJF and **b)** JJA from GISS ModelE2-R using procedure described in text. Stippling highlights areas with anomalies significant at  $p < 0.1$ .

**Figure. 11.** Last Millennium Hovmöller diagram (10 years, time moving forward going upward, with year number labeled next to each month) for **a)** temperature anomaly ( $^{\circ}\text{C}$ ) **b)** precipitation anomaly ( $\text{mm day}^{-1}$ ) using procedure described in text. Solid black lines

mark closest January to start of each eruption used in composite. **c)** Same as panel b, except zoomed in on 10 °S to 10 °N and over 3 years of time beginning with the January closest to each eruption. Red line in panel c shows latitude of maximum climatological precipitation as a function of time of year. All results zonally averaged in model from 77.5°W to 45°W. **d)** Last Millennium Hovmöller diagram for oxygen isotopes in precipitation (per mil).

**Figure. 12.** Frequency distribution of 100 random 45-event composites in LM control simulation of ModelE2-R (blue) for temperature (top row), precipitation (middle), and oxygen isotopes in precipitation (bottom) for DJF (left column) and JJA (right column). Results averaged over same domains as in Figure 9. Normal distribution with a mean and standard deviation equal to that of the data shown in red. Purple square shows the single 45-event composite used in this study, with the distribution of individual 15 volcanic eruptions (each averaged over three ensemble members) in black dots.

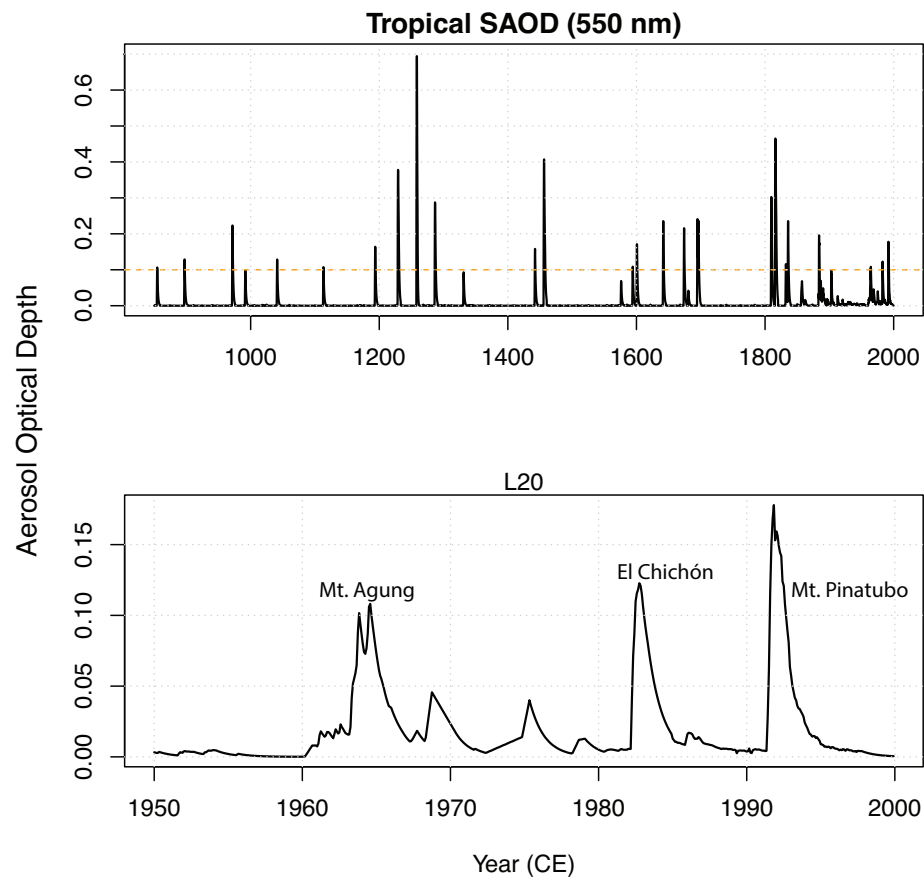


**Figure. 1.** Aerosol Optical Depth (AOD) used to force the NASA GISS ModelE2-R over the Last Millennium and (bottom) zoomed in on the period 1950-1999 (Crowley+Sato) as discussed in text. AOD is the vertically integrated (15-35 km) and latitudinal average from 30°S to 30°N. Note difference in vertical scale between graphs. Orange dashed line marks the AOD threshold for defining a LM eruption in the present study. Eruption events defined in text must sustain the threshold AOD for at least one year, so not all events above the orange dashed line are used in the composites.

## South American Climate System

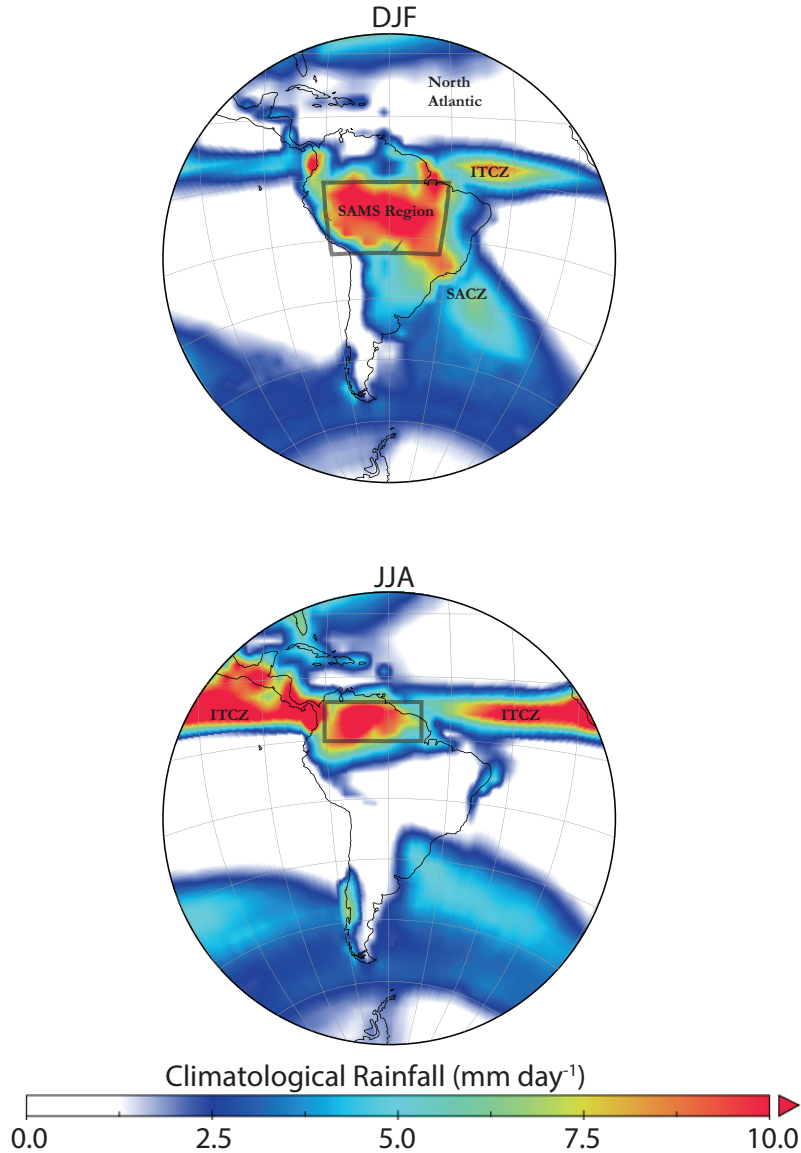


**Figure. 2.** (Top) Observed Climatological Precipitation for DJF (shading, in mm day<sup>-1</sup>). SAMS box is drawn over the domain from [20°S to 0°, 77.5°W to 45°W](#) and used for Figure 9 and 12. Data from the GPCP product, long-term climatological rainfall derived from years 1981 - 2010. (Bottom) As above, except for JJA. Box from [0° to 10°N, 77.5°W to 52.5°W](#) used in averaging for Figures 9 and 12.

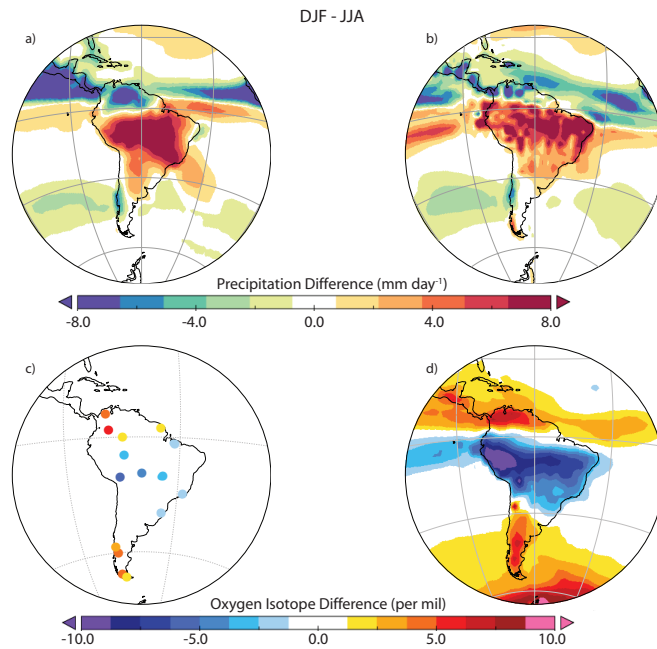


**Figure. 3.** Seasonal cycle (DJF minus JJA) of precipitation in **a)** GPCP precipitation product, from data in Figure 2 **b)** in ModelE2-R **c)**  $\delta^{18}\text{O}_p$  in GNIP data **d)** and  $\delta^{18}\text{O}_p$  in ModelE2-R. GNIP data only shown for stations with at least 90 reported  $\delta^{18}\text{O}_p$  values at a given station from 1960-present, in addition to at least ten data values for each month: December, January, February, June, July, and August. Stations with seasonal differences of less than  $\pm 1.0$  per mil are also omitted in panel (c).

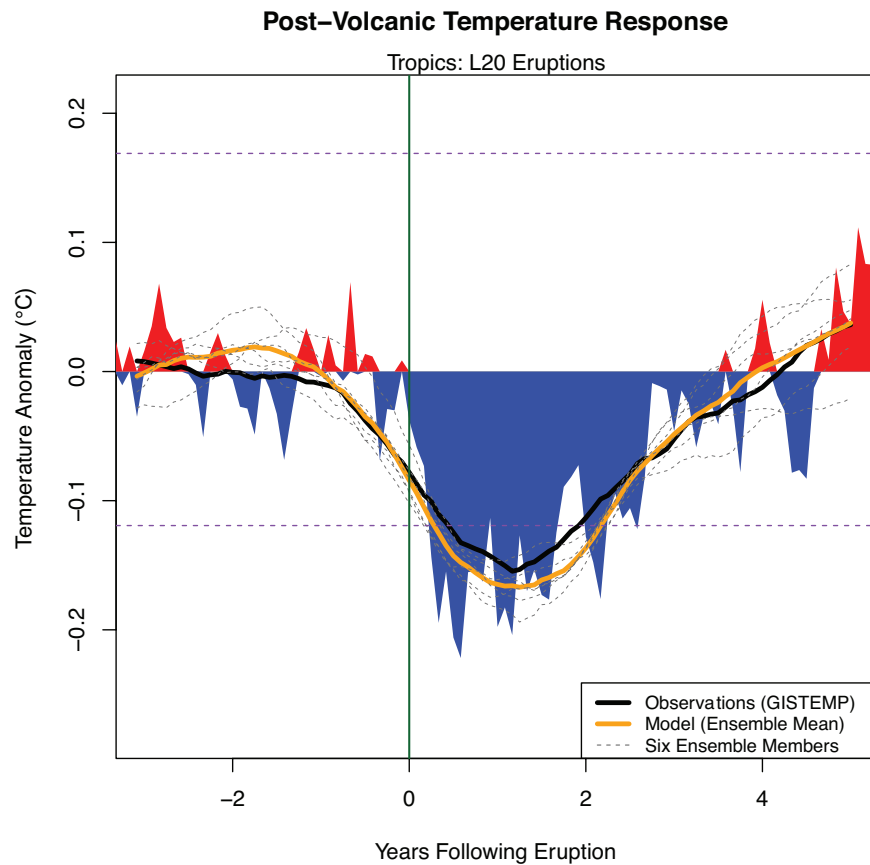


**Figure. 4.** Composite tropical (30°S to 30°N) temperature response following the L20 volcanic eruptions. Fill colors denote observed monthly anomalies using GISTEMP, with 24-month running average shown as solid black line. ModelE2-R ensemble mean is shown as solid orange line and dashed grey lines indicate the six individual ensemble members. Anomalies are referenced to 5 years prior to eruptions (years -5 to 0). Dashed purple lines encompass the 5-95% interval for monthly tropical-mean temperature anomalies (relative to the previous five-year mean) in the GISTEMP product from 1950-present. The calculation of this range omits data two years after the L20 eruptions. The range is not symmetric about zero due to the tropical warming trend during this interval. All data are based on the ENSO-removal technique discussed in text.

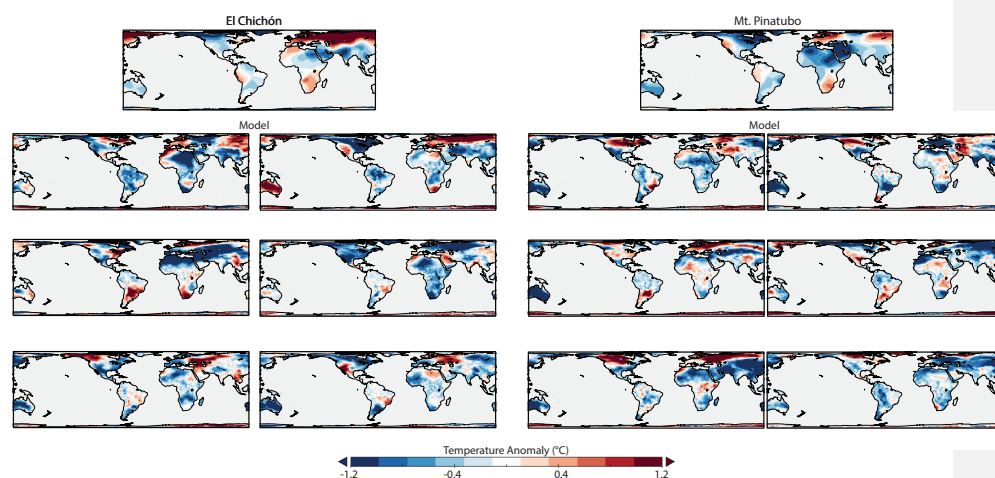


**Figure 5.** Annual-mean temperature change ( $^{\circ}\text{C}$ , ocean masked) for each L20 eruption (labeled on plot) in GISTEMP (top row) and each ModelE2-R ensemble member, as discussed in text. All plots use ENSO-removal procedure described in text.

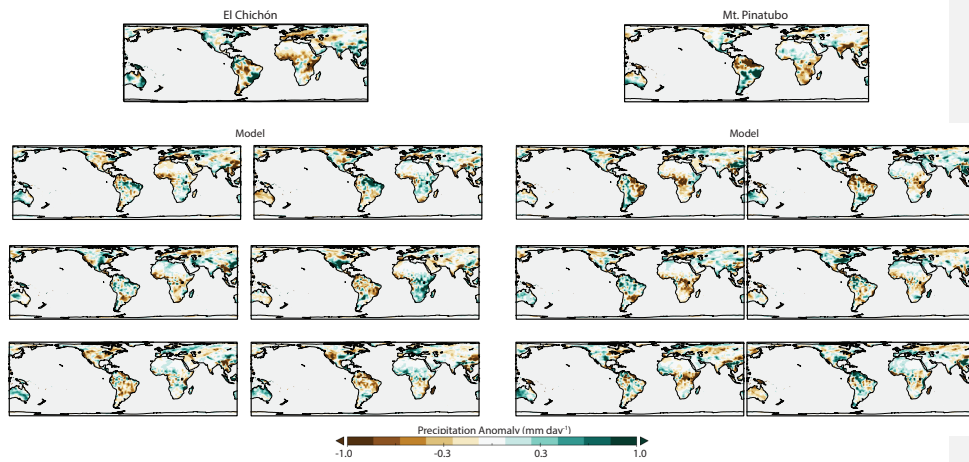


**Figure. 6.** As in Figure 5, except for precipitation change (mm day<sup>-1</sup>).

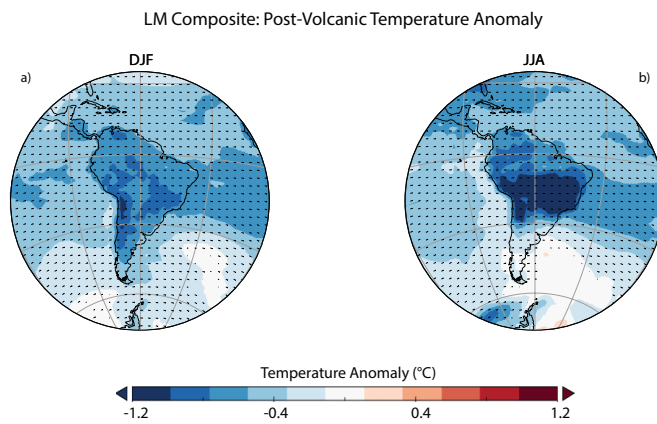


**Figure. 7.** Last Millennium post-volcanic temperature composite ( $^{\circ}\text{C}$ ) averaged over all 45 events during **a)** DJF and **b)** JJA from GISS ModelE2-R using procedure described in text. Stippling highlights areas with anomalies significant at  $p < 0.1$ .

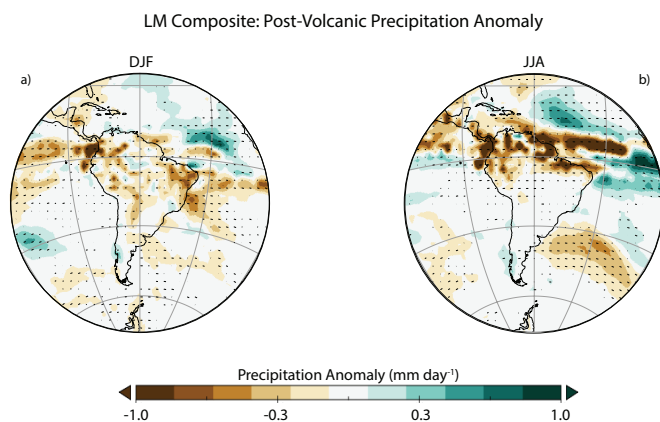


**Figure. 8.** Last Millennium post-volcanic precipitation composite ( $\text{mm day}^{-1}$ ) with all eruption events during **a)** DJF and **b)** JJA from GISS ModelE2-R using procedure described in text. Stippling highlights areas with anomalies significant at  $p < 0.1$ .

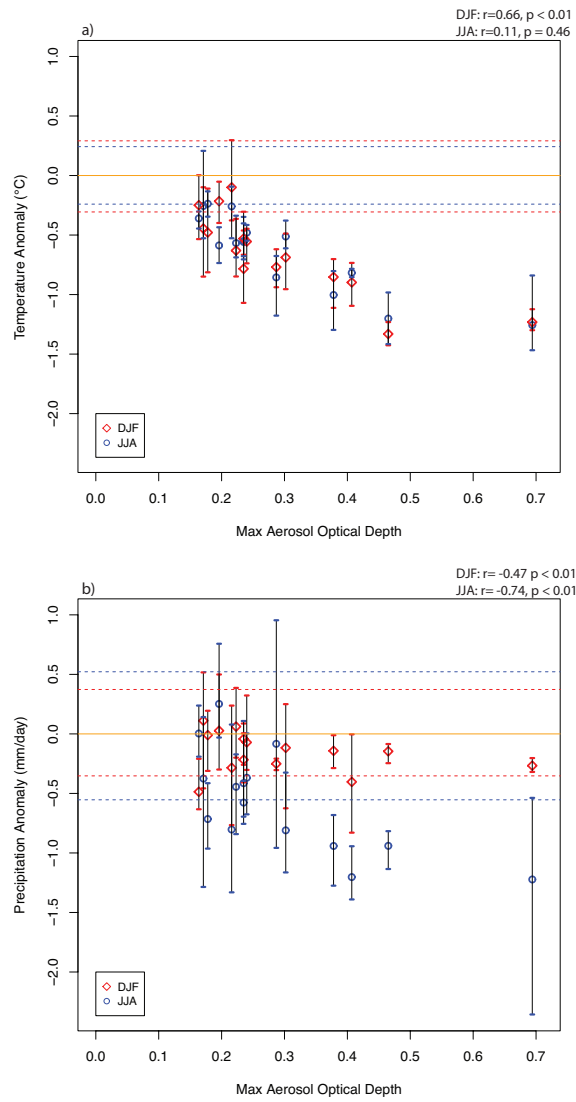
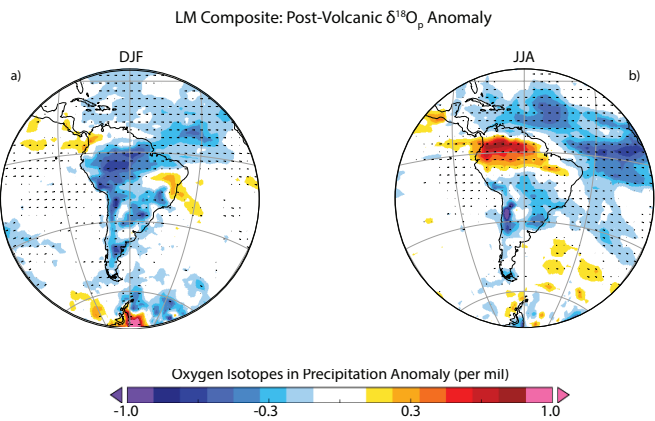


**Figure. 9. a)** Average temperature anomaly during DJF within the SAMS region (red, 20°S to 0°, 77.5°W to 45°W) and equatorial South America during JJA (blue, 0° to 10°N, 77.5°W to 52.5°W) plotted against the peak AOD for all 15 eruptions (each point averaged over three ensemble members with the three member spread shown as horizontal bars) and **b)** As in a), but for precipitation. Dashed horizontal lines indicate the 5-95% range for a two-season average of each variable relative to the previous 15 years (averaged over the same domain) in the entire control simulation with no external forcing. In both panels, the correlation coefficient and p-value are reported for a) temperature and b) precipitation vs.  $\Delta\delta^{18}\text{O}_p$  in each season and over the same domain. The regression uses all 45 volcanic events.



1333  
1334 | **Figure. 10.** Last Millennium post-volcanic oxygen isotope in precipitation ( $\Delta\delta^{18}\text{O}_p$ ) composite  
1335 (per mil) with all eruption events during **a)** DJF and **b)** JJA from GISS ModelE2-R using  
1336 procedure described in text. Stippling highlights areas with anomalies significant at  $p < 0.1$ .  
1337

1338  
1339  
1340  
1341  
1342  
1343  
1344  
1345  
1346  
1347  
1348  
1349  
1350  
1351  
1352  
1353  
1354

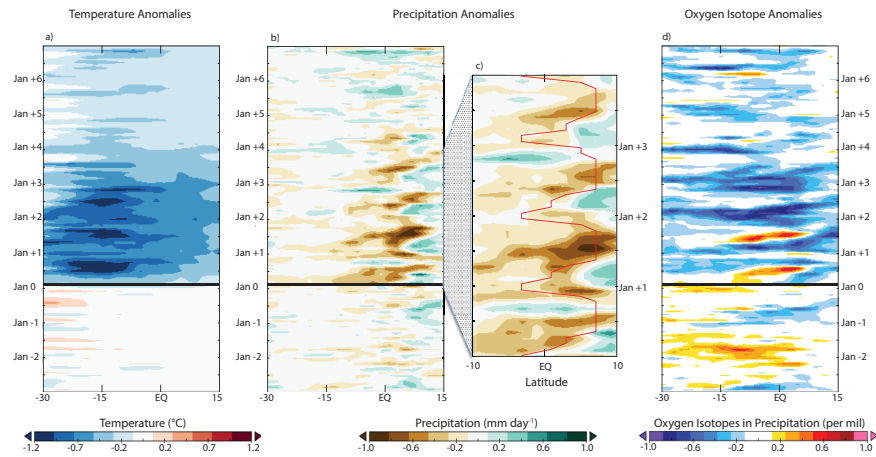
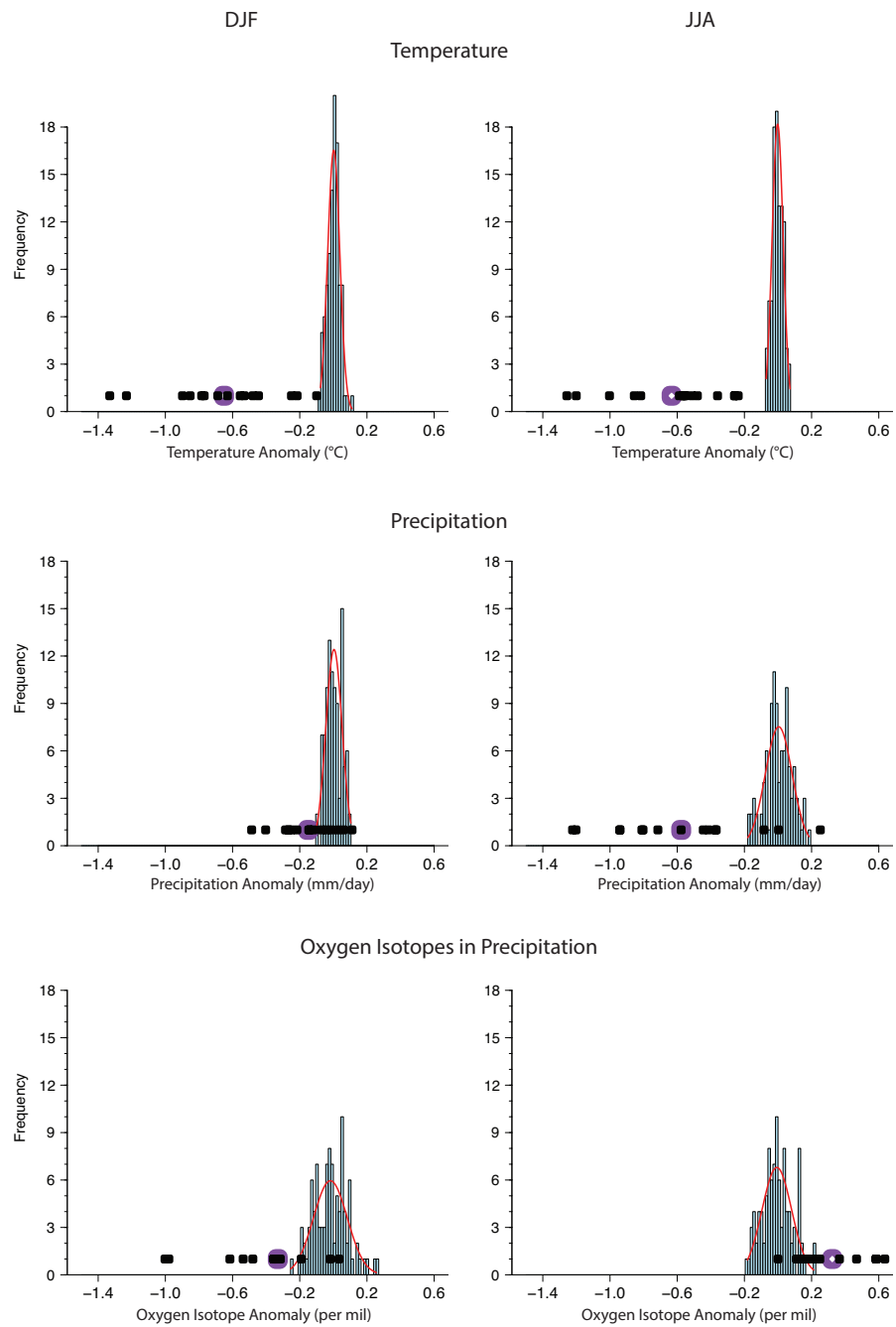


**Figure. 11.** Last Millennium Hovmöller diagram (10 years, time moving forward going upward, with year number labeled next to each month) for **a)** temperature anomaly (°C) **b)** precipitation anomaly (mm day<sup>-1</sup>) using procedure described in text. Solid black lines mark closest January to start of each eruption used in composite. **c)** Same as panel b, except zoomed in on 10 °S to 10 °N and over 3 years of time beginning with the January closest to each eruption. Red line in panel c shows latitude of maximum climatological precipitation as a function of time of year. All results zonally averaged in model from 77.5°W to 45° W. **d)** Last Millennium Hovmöller diagram for oxygen isotopes in precipitation (per mil).



1367

**Figure. 12.** Frequency distribution of 100 random 45-event composites in LM control simulation of ModelE2-R (blue) for temperature (top row), precipitation (middle), and oxygen isotopes in precipitation (bottom) for DJF (left column) and JJA (right column). Results averaged over same domains as in Figure 9. Normal distribution with a mean and standard deviation equal to that of the data shown in red. Purple square shows the single 45-event composite used in this study, with the distribution of individual 15 volcanic eruptions (each averaged over three ensemble members) in black dots.

## Supplemental Figure Captions

**Fig. S1.** Number of rain gauges per grid box for selected months (during eruption events) in the GPCCv6 network. Bottom right panel shows a time-series of the total number of stations over the range 90° to 30° W and 60°S to 20° N.

**Fig. S2.** Zonally averaged latitudinal AOD distribution for all 15 events used in each ensemble member for DJF. Mean of all curves shown in red.

**Fig. S3.** As in Figure S2, but for JJA.

**Fig. S4.** Precipitation anomaly ( $\text{mm day}^{-1}$ ) for each volcanic eruption used in LM composite (each averaged for the three ensemble members used) during DJF.

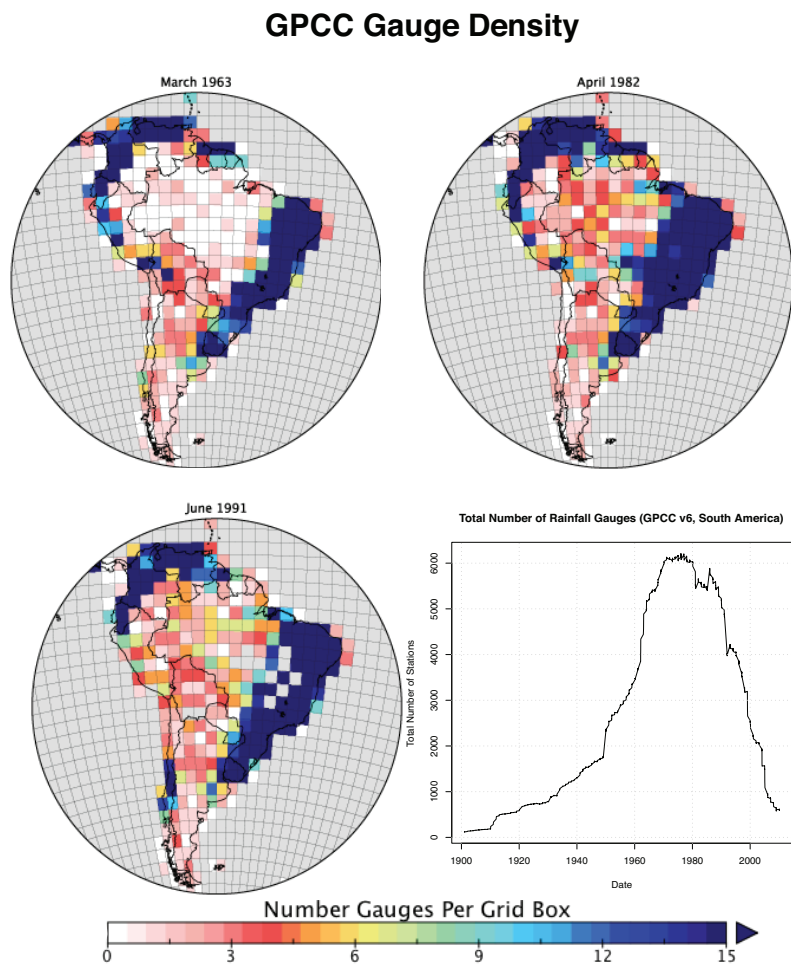
**Fig. S5.** As in Figure S4, but for JJA.

**Fig. S6.** Global-scale precipitation anomaly ( $\text{mm day}^{-1}$ ) in the LM composite for (top) DJF and (bottom) JJA.

**Fig. S7.** Regression of spatially-averaged DJF  $\delta^{18}\text{O}_p$  anomaly vs. temperature (black squares) or precipitation (red squares). The regression uses all 45 LM volcanic events and averaging is done over the SAMS domain defined in the text. Black and red lines are the corresponding (least-squares) regression lines.

**Fig. S8.** **a)** DJF total  $\delta^{18}\text{O}_p$  anomaly **b)** DJF  $\delta^{18}\text{O}_p$  anomaly due to isotopic composition change in precipitation, holding precipitation seasonality fixed at pre-eruption values. **c)** As in a) except for JJA. **d)** As in b) except for JJA. Total isotopic changes in left column reproduced from Figure 10 in text.

1412  
1413  
1414  
1415



1416  
1417 **Fig. S1.** Number of rain gauges per grid box for selected months (during eruption events)  
1418 in the GPCCv6 network. Bottom right panel shows a time-series of the total number of  
1419 stations over the range 90° to 30° W and 60°S to 20° N.  
1420

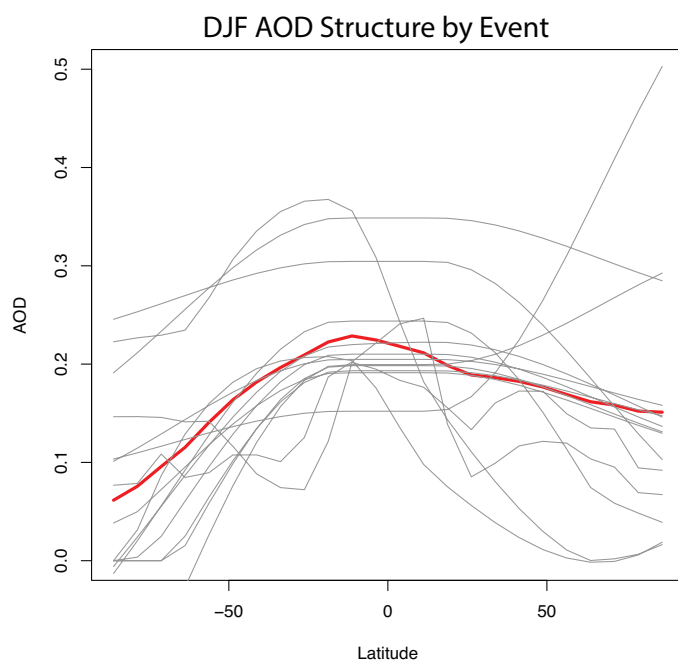


**Fig. S2.** Zonally averaged latitudinal AOD distribution for all 15 events used in each ensemble member for DJF. Mean of all curves shown in red.

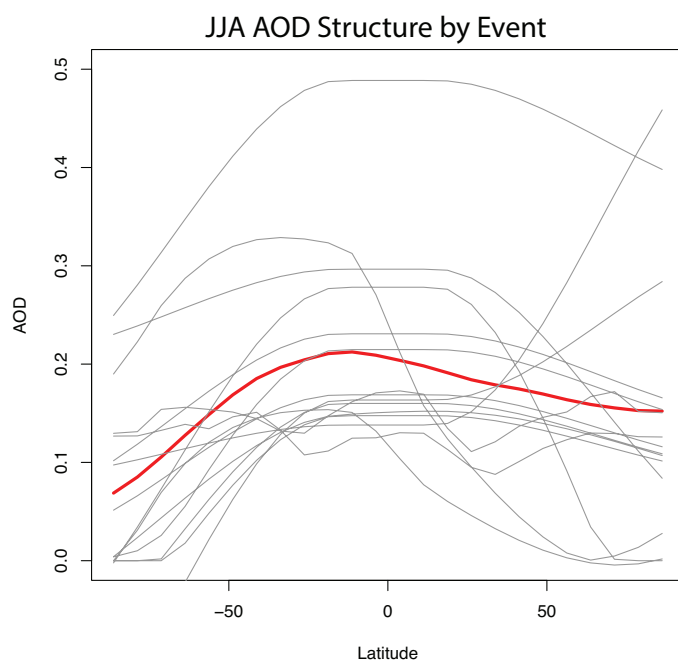


**Fig. S3.** As in Figure S2, but for JJA.

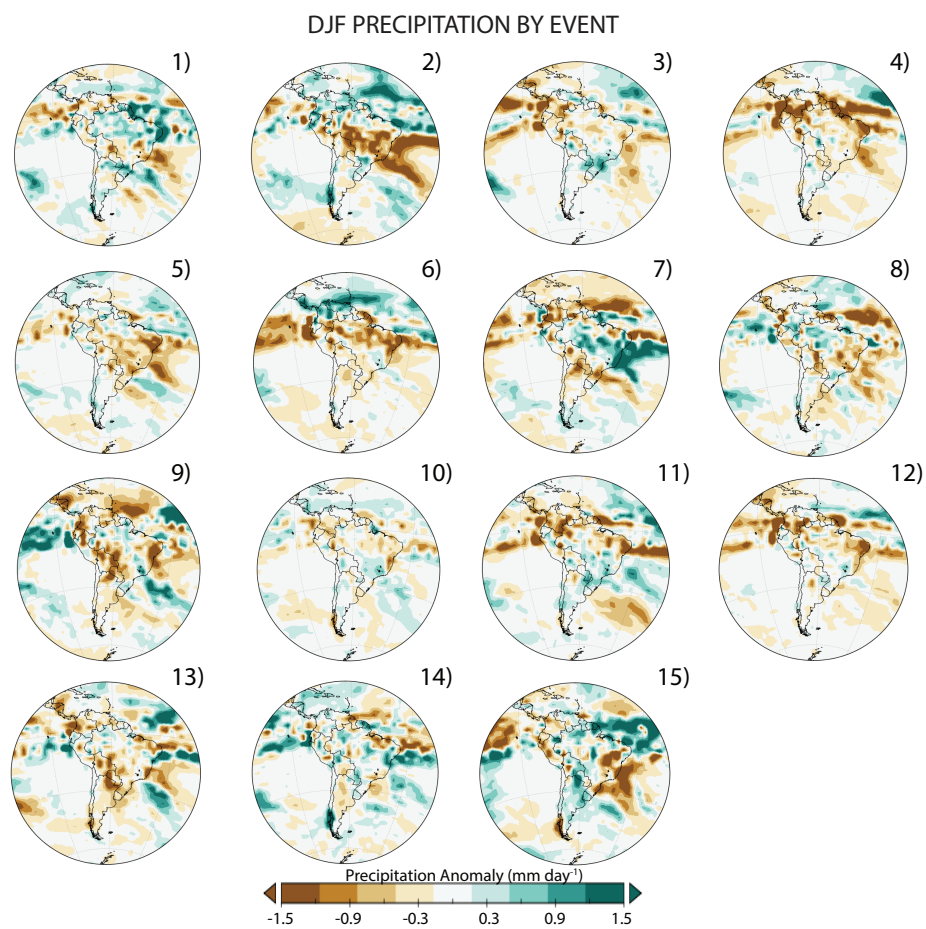


**Fig. S4.** Precipitation anomaly ( $\text{mm day}^{-1}$ ) for each volcanic eruption used in LM composite (each averaged for the three ensemble members used) during DJF.

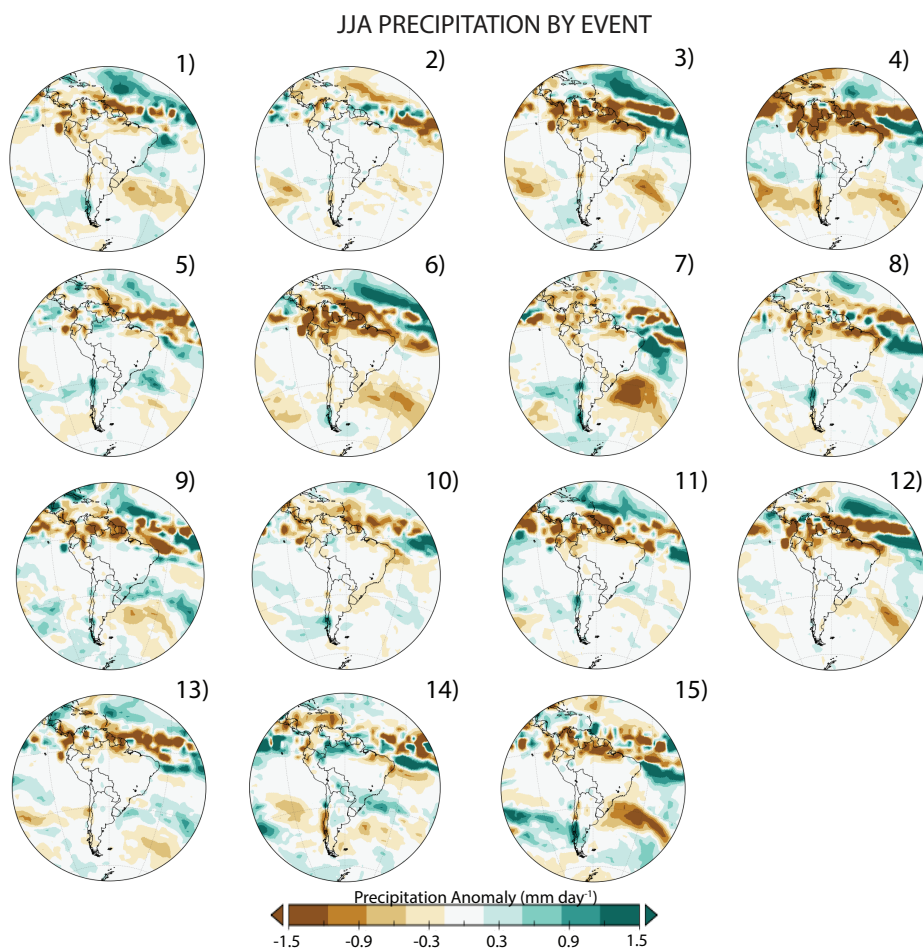


**Fig. S5.** As in Figure S4, but for JJA.

## Global LM Precipitation Anomaly Composite

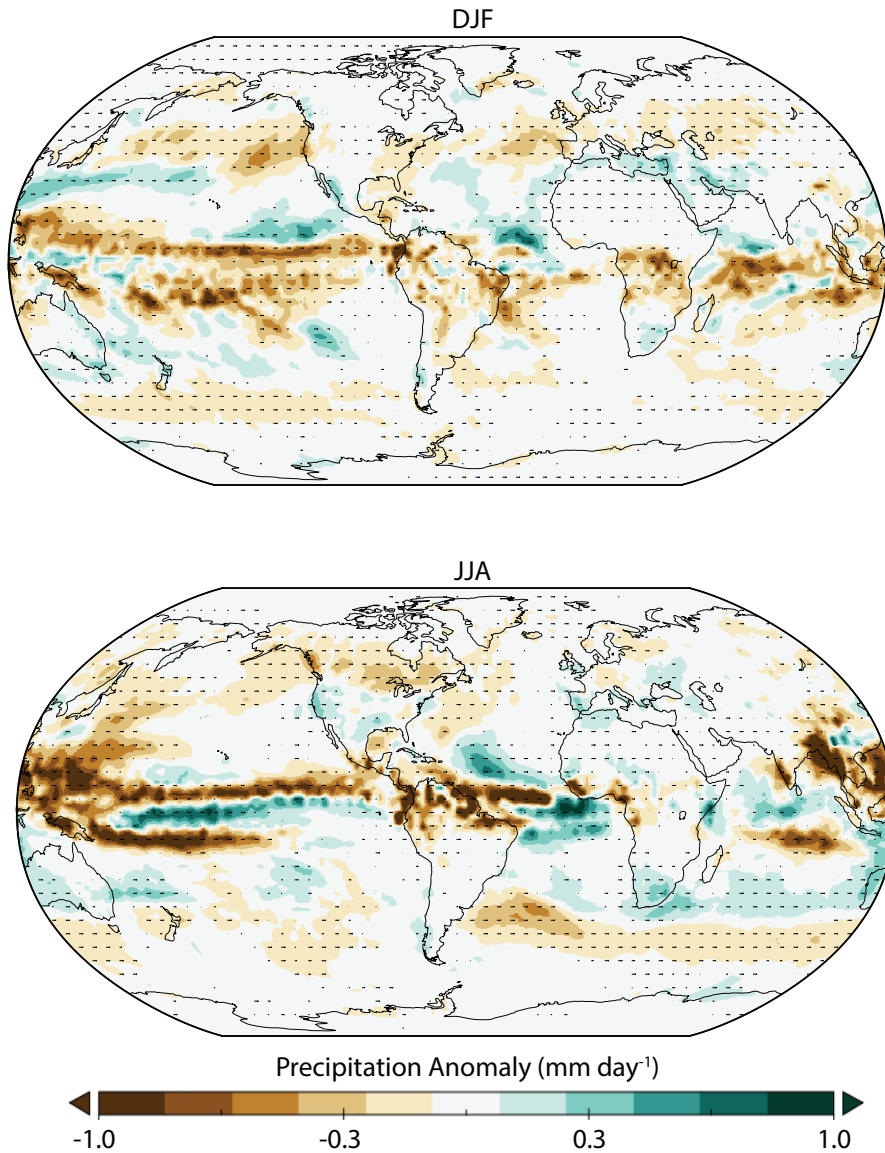


**Fig. S6.** Global-scale precipitation anomaly (mm day<sup>-1</sup>) in the LM composite for (top) DJF and (bottom) JJA.

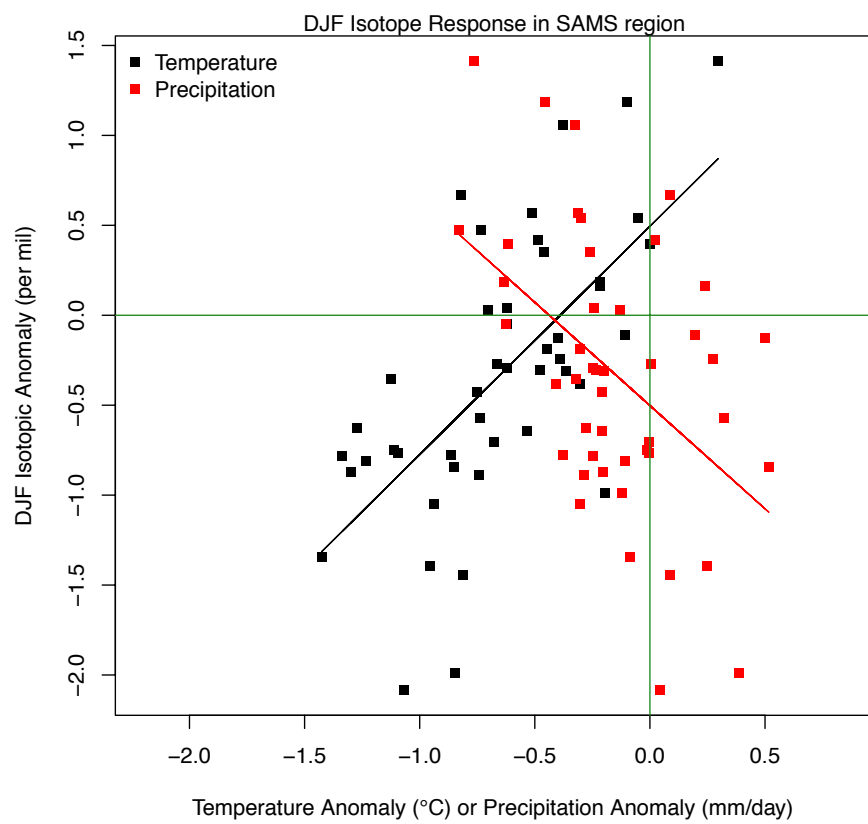


**Fig. S7.** Regression of spatially-averaged DJF  $\delta^{18}\text{O}_p$  anomaly vs. temperature (black squares) or precipitation (red squares). The regression uses all 45 LM volcanic events and averaging is done over the SAMS domain defined in the text. Black and red lines are the corresponding (least-squares) regression lines.

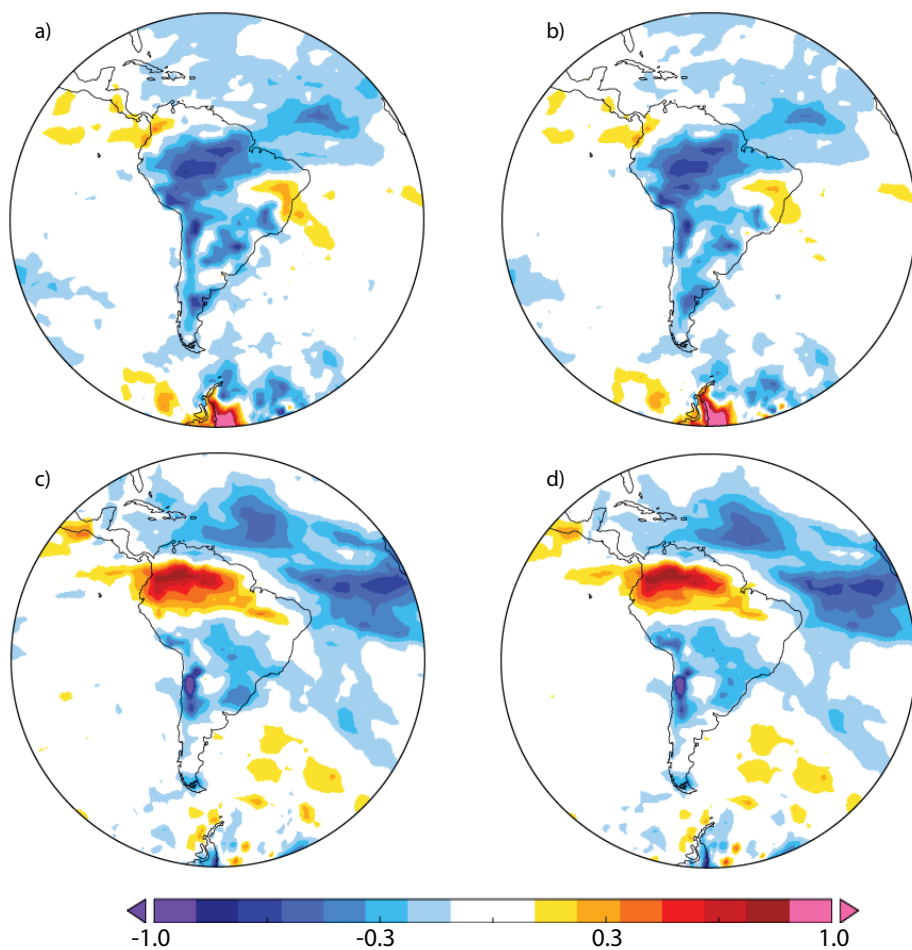


**Fig. S8.** **a)** DJF total  $\delta^{18}\text{O}_p$  anomaly **b)** DJF  $\delta^{18}\text{O}_p$  anomaly due to isotopic composition change in precipitation, holding precipitation seasonality fixed at pre-eruption values. **c)** As in a) except for JJA. **d)** As in b) except for JJA. Total isotopic changes in left column reproduced from Figure 10 in text.